

REPORT DOCUMENTATION PAGE

AFRL-SR-AR-TR-05
O 10

The public reporting burden for this collection of information is estimated to average 1 hour per response, including the time gathering and maintaining the data needed, and completing and reviewing the collection of information. Send comments regarding the burden reduction to Department of Defense, Washington Headquarters, Suite 0704-0188, 1215 Jefferson Davis Highway, Suite 1204, Arlington, VA 22202-4302. Respondents should be aware that they are subject to any penalty for failing to comply with a collection of information if it does not display a currently valid OMB control number.

PLEASE DO NOT RETURN YOUR FORM TO THE ABOVE ADDRESS.

1. REPORT DATE (DD-MM-YYYY) 15072004			2. REPORT TYPE Final Report		3. DATES COVERED (From - To) 01 Jan 2001 - 30 Jun 2004	
4. TITLE AND SUBTITLE Modeling of Damage Micromechanisms in Structural Ceramic Matrix Composite Under Static and Cyclic Loading			5a. CONTRACT NUMBER			
			5b. GRANT NUMBER F49620-01-1-0143			
			5c. PROGRAM ELEMENT NUMBER			
6. AUTHOR(S) Professor Kenneth W. White			5d. PROJECT NUMBER			
			5e. TASK NUMBER			
			5f. WORK UNIT NUMBER			
7. PERFORMING ORGANIZATION NAME(S) AND ADDRESS(ES) Department of Mechanical Engineering University of Houston Houston TX 77204-4792				8. PERFORMING ORGANIZATION REPORT NUMBER		
9. SPONSORING/MONITORING AGENCY NAME(S) AND ADDRESS(ES) USAF/AFRL AFOSR 801 N. Randolph Street Arlington VA 22203 <i>NA</i>				10. SPONSOR/MONITOR'S ACRONYM(S) AFOSR		
				11. SPONSOR/MONITOR'S REPORT NUMBER(S)		
12. DISTRIBUTION/AVAILABILITY STATEMENT Distribution Statement A. Approved for public release; distribution is unlimited.						
13. SUPPLEMENTARY NOTES						
14. ABSTRACT A unique experimental procedure was used to determine crack bridging stresses, as well as the fiber/matrix interfacial role during fiber sliding and as an active energy dissipation mechanism in fiber-reinforced ceramic matrix composites with all-oxide constituents. A displacement-controlled failure mechanism dominates in these composites, establishing a useful relationship between accumulated damage and present crack opening displacements for failure prediction under fatigue loading conditions. Microstructural analysis by SEM led to identification of important changes with temperature exposure, allowing the determination of critical service temperatures. Using the LEFM model, values for fracture toughness comparable to those of some metals were found for these composites						
15. SUBJECT TERMS						
16. SECURITY CLASSIFICATION OF: a. REPORT U b. ABSTRACT U c. THIS PAGE U			17. LIMITATION OF ABSTRACT UU	18. NUMBER OF PAGES 71	19a. NAME OF RESPONSIBLE PERSON 19b. TELEPHONE NUMBER (Include area code)	

MODELING OF FAILURE IN MONOLITHIC AND CERAMIC MATRIX COMPOSITE
UNDER STATIC AND CYCLIC LOADING

Supported by the
Air Force Office of Scientific Research
Grant Number F49620-01-1-0143
Subrecipient Agreement #1551083/3913/K155031

Final Report

INVESTIGATION AND MODELING OF FAILURE MICROMECHANISMS IN
MONOLITHIC AND REFRACTING CERAMIC MATRIX COMPOSITE
UNDER STATIC AND CYCLIC LOADING

July 15, 2004

College of Engineering
UNIVERSITY OF WASHINGTON

20050322 387

ACKNOWLEDGEMENT

The results generated in this report were made possible by a third three-year funding from the Air Force Office of Scientific Research through a subcontract from the University of Houston. The author wishes to express his sincere gratitude to the Air Force Office of Scientific Research and to Professor Kenneth W. White for their continuous support during this period. The all-oxide continuous fiber ceramic composite plates were provided by Professor F. W. Zok, University of California, Santa Barbara. The results reported here would not have been possible without the dedicated work of Dr. Junji Ohgi, Visiting Scientist, Yamaguchi University and Mr. Piotr Stegawski, MS student in the Department of Mechanical, University of Washington.

University of Washington

ABSTRACT

INVESTIGATION AND MODELING OF FAILURE MICROMECHANISMS IN MONOLITHIC AND REFRACTING CERAMIC MATRIX COMPOSITE UNDER STATIC AND CYCLIC LOADING

By Albert S. Kobayashi

A third generation, 2-D finite element (FE) model of grain pull-out was formulated by incorporating frictional sliding, intact elastic grain bridging and cantilevered grains of the second-generation model into the first generation finite element model of five parallel, planar arrays of two-dimension, uniform grains. Frictional resistance due to grain boundary sliding was generated by the inter-granular compressive stress due to randomly distributed, anisotropic thermal contraction during cool down in the fabrication process. This third generation model faithfully duplicated the measured crack bridging force versus crack opening displacement relation in a loaded and unloaded alumina wedge-loaded double cantilever beam (WL-DCB) specimen. Optimization study based on the crack bridging forces showed that alumina with all 5 μm grain provided the largest K_{IC} of 3.4 MPa $\sqrt{\text{m}}$ and 2.81 MPa $\sqrt{\text{m}}$ at room temperature and 800°C, respectively.

Fracture behavior of carbon fiber/carbon matrix (C/C) composite was then analyzed with a 2-D FE model of a single edged notch bend (SENB) specimen subjected to a series of re-notching tests. The irregular transverse cracking in the wide frontal fracture process zone (FPZ) of the machined notch tip was represented by an idealized distribution of crack bridging stress (CBS) along an idealized straight crack. The CBS was obtained through an inverse analysis by matching the FE computed and moiré measured crack opening displacement (COD) during the re-notching process. This FE model was used to estimate the equivalent strain energy release rate, G_{eq} , and the equivalent stress intensity factor, K_{eq} , of the zig-zagged crack.

Finally, crack bridging forces in an all-oxide, continuous fiber ceramic composite (CFCC), single edge notch (SEN) specimen with fixed grip loading were determined by an inverse, hybrid experimental-numerical procedure. The SEN specimen was machined from a 12-ply, laminated woven Nextel 720 fibers in a mullite/alumina matrix composite. The irregular and non-symmetric crack opening profiles were recorded photographically or by moiré interferometry. A 2-D orthotropic elastic FE model of the SEN specimen, together with the crack opening profile, was used in its propagation mode to determine the crack bridging stress under crack growth. The resultant crack bridging stress was in good agreement with that determined by post fracture tension (PFT) tests.

TABLE OF CONTENT

List of Figures	5
Introduction	7
Chapter 1 Optimum Grain Size for Polycrystalline Alumina	9
1.1. Crack Closure Stress	9
1.2. FE Model	9
1.3. Results	13
1.4. Conclusion	17
Chapter 2 A FE Model of Carbon/Carbon Composite Fracture	18
2.1 Hybrid Moiré-FE Analysis	18
2.1.1 Single-edged Notch Bend (SENB) Specimen	18
2.1.2 Three-point Bend Test	19
2.1.3. Re-notching Test	21
2.1.4. Moiré Interferometry	23
2.1.5. Finite Element Modeling	24
2.2. Results	24
2.3. Conclusions	27
Chapter 3 Crack Bridging Force in Mullite/Alumina Composite	28
3.1. All Oxide Composite	28
3.2. Experimental Procedure	28
3.2.1. SEN Specimen	28
3.2.2. Fracture Test	29
3.2. Numerical Model	36
3.3. Results	37
3.3.1. CFCC-A SEN Specimen	37
3.3.2. CFCC-B SEN Specimen	39
3.4. Discussion	42
3.5. Conclusion	42
Chapter 4 Conclusions and Recommendation	43
References	44

LIST OF FIGURES

Fig. 1.1. Intergranular and transgranular grain fracture.	9
Fig. 1.2. Fractured bridging grain.	9
Fig. 1.3. Parallel assembly of five grain arrays.	10
Fig. 1.4. Two-dimension FE model of uniform grain size.	11
Fig. 1.5. Grain bridging model.	11
Fig. 1.6. CCS versus COD relations at 800°C.	12
Fig. 1.7. CCS versus COD relations at room temperature.	13
Fig. 1.8. CCS vs. COD relations during the first loading and unloading at room temperature.	14
Fig. 1.9. CCS vs. COD relations during the first loading and unloading at 800° C.	14
Fig. 1.10. Variation of Mises stress distribution along the crack at maximum load. ($T = 800^\circ\text{C}$, grain size=15 μm .)	15
Fig. 1.11. Variation in CCS at maximum applied displacement at 800°C.	16
Fig. 1.12. Variation in CCS at maximum applied displacement at room temperature.	16
Fig. 1.13. Crack closure stress intensity factor for each grain size.	17
Fig. 2.1. C/C composite.	18
Fig. 2.2. C/C composite SENB specimen.	19
Fig. 2.3. Crack path and fractured C/C SENB specimen.	20
Fig. 2.4. Load versus load-line displacement with crack growth. C/C SENB specimen.	20
Fig. 2.5. Stress intensity factor of a straight crack in a C/C SENB specimen.	21
Fig. 2.6. Stress intensity factor at crack growth initiation and maximum load.	21
Fig. 2.7. Load versus load-line displacement relation of re-notched C/C SENB specimen.	22
Fig. 2.8. High temperature moiré interferometry setup.	22
Fig. 2.9. Actual FPZ and moiré pattern.	23
Fig. 2.10. FE model of the re-notched C/C SENB specimen.	24
Fig. 2.11. COD profiles.	25
Fig. 2.12. Crack bridging stress.	25
Fig. 2.13. Reduction in bridging stress intensity factor.	26
Fig. 2.14. G_I versus K_I .	27
Fig. 3.1. SEN specimen.	29
Fig. 3.2. Fractured SEN specimen with CMOD gage attached.	29
Fig. 3.3. Photo of fractured specimen. Back side of a CFCC-B SEN specimen.	30
Fig. 3.4. Fiber pullout I. CFCC-B specimen.	30
Fig. 3.5. Fiber pullout II. CFCC-B specimen.	31
Fig. 3.6. Load versus CMOD. CFCC-A SEN specimen under monotonic loading.	31
Fig. 3.7. Crack opening profile of CFCC-A SEN specimen.	32
Fig. 3.8. Load versus CMOD of monotonic loaded CFCC-B SEN specimen.	33
Fig. 3.9. Moiré interferometry bench.	33
Fig. 3.10. Moiré interferometry bench with light beams marked.	34
Fig. 3.11. Moiré interferometry image. Front side of CFCC-B SEN specimen.	34
Fig. 3.12. Load versus CMOD of a cyclic loaded CFCC-B SEN specimen.	35

Fig. 3.13. Load versus CMOD of monotonic and cyclic loaded CFCC-B SEN specimens.	35
Fig. 3.14a. FE model of SEN specimen with clamped grips.	36
Fig. 3.14b. FE model of SEN specimen.	36
Fig. 3.15. Crack opening profile with crack extension. CFCC-A SEN specimen under monotonic loading.	37
Fig. 3.16. Crack bridging stress versus COD relations of a CFCC-A SEN specimen under monotonic loading.	38
Fig. 3.17. Enlarged section of Figure 3.16. CFCC-A SEN specimen.	38
Fig. 3.18. Crack opening profile with crack extension of a monotonic loaded CFCC-B SEN specimen.	39
Fig. 3.19. Crack bridging stress versus COD relations of a monotonic loaded CFCC-B SEN specimen.	40
Fig. 3.20. Measured and computed COD in a monotonic loaded CFCC-B SEN specimen.	40
Fig. 3.21. Crack opening profile of a cyclic loaded CFCC-B SEN specimen.	41
Fig. 3.22. Crack bridging stress versus COD in a cyclic loaded CFCC-B SEN specimen.	42

INTRODUCTION

Since the earlier work of Kneehans et. al. [1], numerous analyses on the toughening effects generated by grain bridging in the trailing fracture process zone (FPZ) have been published over the past decade. Unfortunately, the controlling factor, the grain bridging force was only inferred in the majority of studies. Hay and White [2] used a "post fracture tension" (PFT) specimen to directly measure the crack closure stresses (CCS) in the trailing wake of a stably grown crack in a high purity alumina, wedge-loaded double cantilever beam (WL-DCB) specimen. The PFT results provided an excellent platform for modeling the grain-bridging force due to frictional sliding since other grain bridging mechanisms such as elastic grain bridging and cantilevered grain rotation occurred in the frontal FPZ of a crack tip. A zeroth order finite element (FE) model of the PFT specimen subjected to monotonic loading by Tran, et. al. [3] provided the load versus displacement results which were in remarkable agreement with the measured results of Hay and White [2]. This model was followed by a first order FE model [4] of a cyclic loaded PFT specimen and by a second order FE model [5, 6] of grain bridging in a cyclic loaded WL-DCB specimen. In the following Chapter 1, an estimate of the optimum grain size based on a micro-mechanic FE model of grain pullout in polycrystalline alumina is presented.

Self similar crack growth in a fiber reinforced composite is seldom observed due to the inevitable crack deflection along debonded fibers, interply delamination as well as fabrication defects in the crack path. While the overall crack growth direction is perpendicular to the local maximum stress direction, the tortuous 3-D crack path poses an insurmountable challenge for a linear elastic fracture mechanics (LEFM) interpretation of crack growth in a fiber reinforced composite. Numerous attempts have been made to quantify composite fracture through the micromechanics in the trailing FPZ involving fiber pullout, fiber breaking, matrix cracking and interply delamination. The interaction of these micro- and macro-mechanic failure mechanisms, unfortunately, overwhelms a LEFM analysis. Never the less LEFM, has been used successfully in assessing the onset of crack growth of a straight machined crack with a relatively small FPZ by lumping the micro-mechanic failure modes into a single energy dissipation mechanism.. This continuum approach, however, is no longer valid when the FPZ is more than ten percent of the original crack length. As an alternative, nonlinear fracture mechanics, such as J -integral, has been used to estimate the fracture resistance of fiber reinforced ceramic composite after replacing the zig-zagged crack with a "linear crack [7]". Another approach is to measure directly the crack bridging stress generated by the zig-zagged crack with the post fracture tension (PFT) method [8] or indirectly by the re-notching method [9]. In Chapter 2, a LEFM model of the complex failure mechanism is modeled with a postulated self-similar crack extension. The LEFM model of the frontal FPZ is assumed to be a straight cohesive zone with a crack bridging force which replaces the multifaceted failure mechanisms. The bridging force is determined by a hybrid moiré-finite element (FE) analysis. With this simplified 2-D modeling, LEFM can then be used to characterize stable crack growth in a fiber reinforced composite.

The third topic involves fracture of an all ceramic composite. Since ceramic composites lack any sizable plastic zone at the crack tip, alternate fracture energy

dissipation mechanisms have been the subject of intense studies during the past twenty years. Matrix cracking ahead of the crack tip, crack deflection at the matrix-fiber interface and fiber bridging along a crack are all energy dissipation mechanisms, which act independently, concurrently or interactively, in ceramic matrix composites. In terms of experimental analysis, numerous attempts have been made to quantify these mechanisms and their contributions to the overall perceived fracture toughness of ceramic matrix composites. An alternate to above, is to lump the three mechanisms into a simple model of a FPZ trailing the crack tip and to estimate the energy dissipated in this FPZ. This idealized model is based on LEFM where the measured crack opening profile is input to a 2-D orthotropic elastic finite element (FE) model of a fracture specimen from which the crack bridging force is obtained. The observed complex and non-symmetric crack opening profiles on two sides of a composite specimen, particularly that of a laminated composite with woven fiber structure, however, renders this straight forward hybrid experimental-numerical analysis impractical. Thus an inverse analysis was used in Chapter 3 to estimate the crack bridging force in the FPZ of an all oxide composite.

CHAPTER 1 OPTIMUM GRAIN SIZE FOR A POLYCRYSTALLINE ALUMINA

1.1 Crack Closure Stress

Abundant experimental evidence shows that the dominant fracture energy dissipation mechanism in structural ceramics is the crack opening resistance in the trailing FPZ of a crack. The FE model described in [3, 4] simplifies the complex micro-mechanics governing grain separation along the opening crack to load and displacement boundary conditions. A slightly different version of this hybrid analysis was performed to determine the crack closure stress (CCS) at room temperature and 800°C during periods of loading and unloading [6]. The observed decrease in the crack bridging force at 800°C was attributed to both the decrease in viscosity of the glassy grain interface and the partial relief of the residual compressive stresses, both of which contribute to a decrease in the resistance to grain pull out.

1.2. FE Model

A micromechanical model based on all three grain bridging mechanisms of frictional sliding, intact elastic grain bridging and cantilevered grains, as shown in Figures 1.1 and 1.2, of the second-generation model [5, 6] was incorporated into the first generation finite element model of five parallel, two-dimensional, uniform grain arrays [3]. A parallel assembly of the five two-dimensional arrays of five different grain sizes is shown in Figure 1.3. Since the model was a slice through the thickness of the wedge-loaded, double cantilever beam (WL-DCB) specimen, the width of the FE model was equal to the thickness of the WL-DCB specimen minus the side groove or 2.4 mm. This third generation micromechanical model of the alumina WL-DCB specimen was subjected to load and unload and the numerical results were compared with the experimental results.

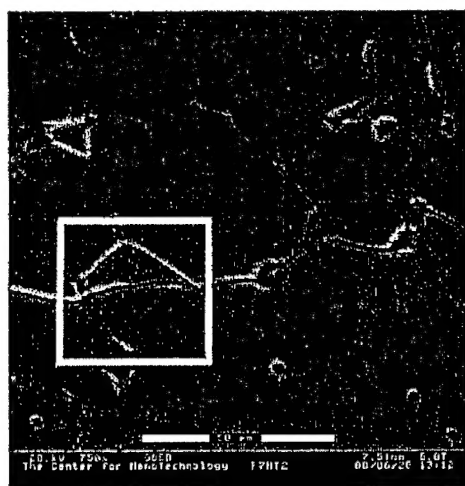


Fig. 1.1. Intergranular and transgranular grain fracture.

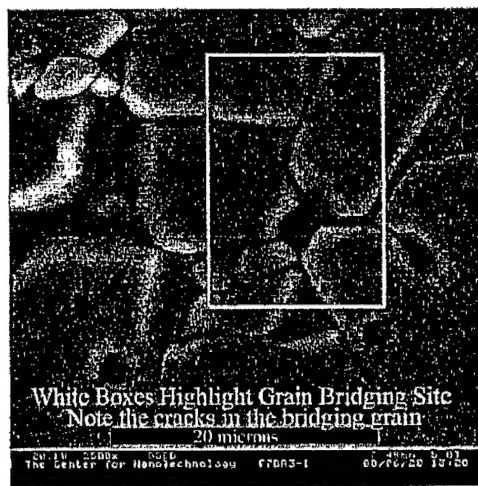


Fig. 1.2. Fractured bridging grain.

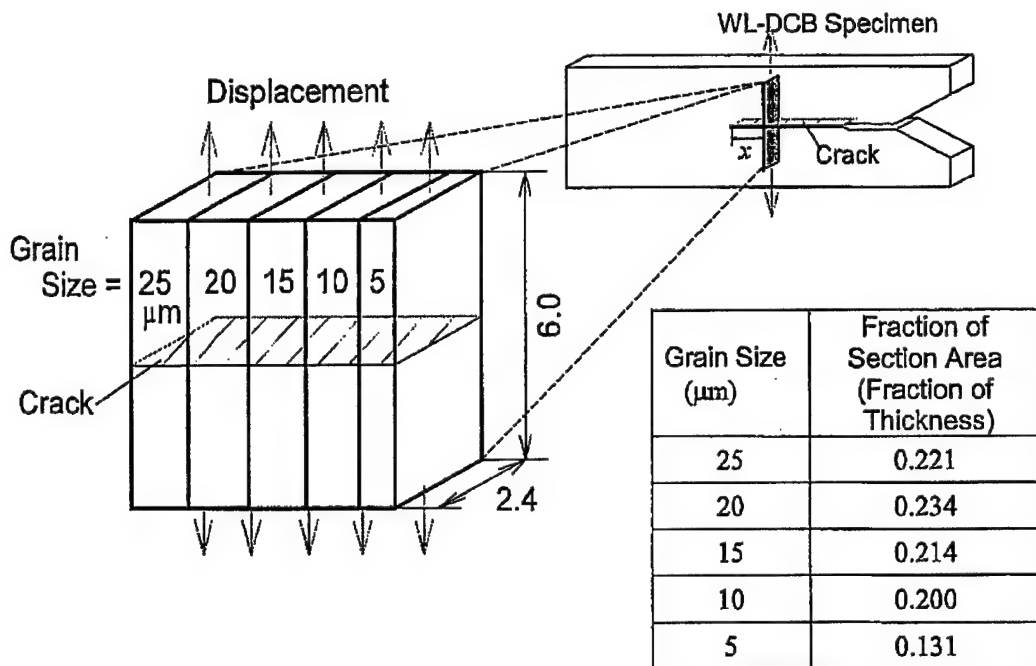


Fig. 1.3. Parallel assembly of five grain arrays.

Figure 1.4 shows the FE model of a panel array of constant grain size. The disposable parameters in this panel were the relative contributions of elastic grain bridges, cantilevered grains, frictional bridging and the grain bridging force as shown in Figure 1.5 [6]. By necessity, the model was a highly idealized assembly of quadrilateral elements. At the interface, elastic grain bridges were modeled by constraining the coincident nodes on the opposite side of the crack to have the same displacement. Angled, cantilevered grains were modeled by adjusting the nodal points of the initial mesh to provide an angled interaction surface. Frictional bridges were modeled, as in the previous cases, with the frictional properties defined at the crack interface. Lacking any prior analysis of the behavior of the grain bridges during loading, a time consuming trial-and-error, iterative, inverse analysis was used to match the meso-responses of the micro-mechanical model and the experimental data, primarily the applied load, crack opening displacement (COD) profile and CCS vs. COD relation.

A Matlab preprocessor randomly distributed the principal thermal expansion directions from 0 to 165° in 15° increments. As shown in Figure 1.5, the principal direction in the bridging element was assumed to be identical with that of an adjoining element. The compressive residual stress, which caused frictional resistance to the grain pullout, was generated by the mismatch in grain shrinkage during the cool down from the processing temperature. Grain sizes smaller than $3 \mu\text{m}$ were considered too small for effective grain bridging in the WL-DCB specimen.

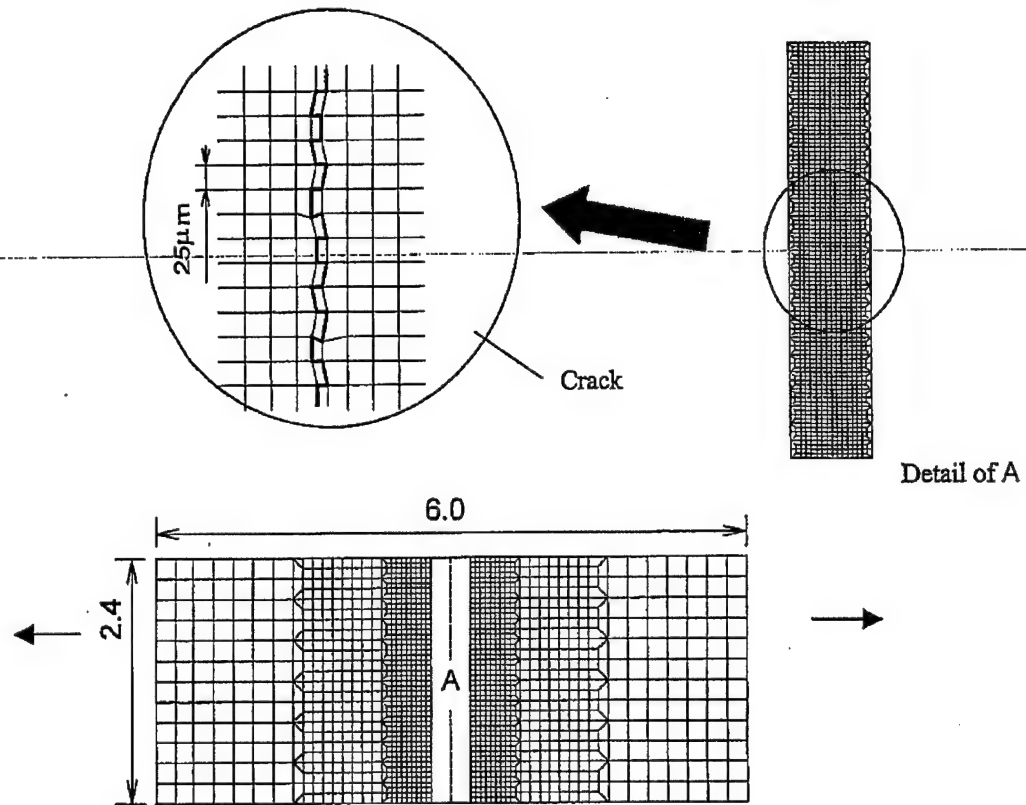


Fig. 1.4. Two-dimension FE model of uniform grain size.

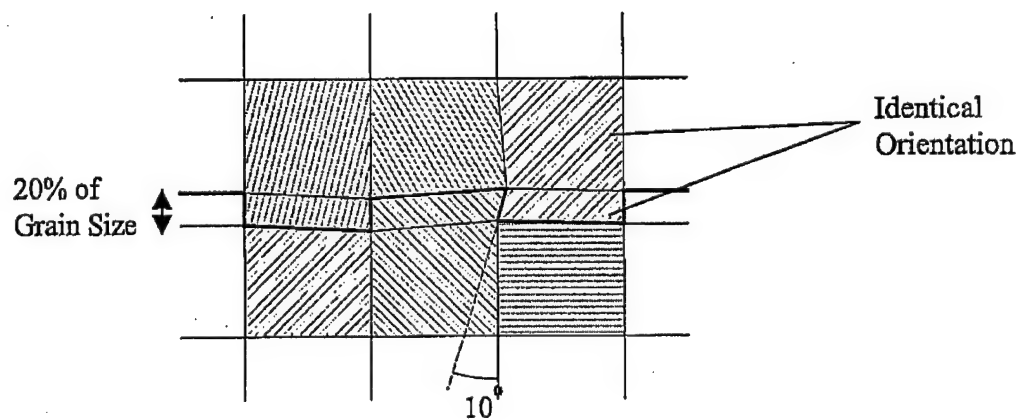


Fig. 1.5. Grain bridging model.

The frictional bridging length was assumed to be 20 percent of the grain length, e.g. 5 μm for the 25- μm size grain. The cantilevered element was assumed to be tilted 10° to the loading direction. The number of elastic and cantilevered grain bridging along the trailing fracture process zone was assumed to be equal and proportional to the number of grains along the fracture surface of each panel of grains in Figure 1.5. This proportionality constant was determined through an inverse analysis by matching the average slope of the CCS versus COD relation of the parallel assembly of the five grain panels with the observed experimental results. Figures 1.6 and 1.7 show the individual CCS versus COD relations for the five panels of grains as well as the average and the measured CCS versus COD relations at 800°C and at room temperature, respectively. Specifically, elastic and cantilever grain bridging sites occurred in ten grains in the panel of 15 μm grains while this number was six grains for the panel of 25 μm grains at 800°C. Thus, the proportionality constant involving the numbers of elastic to cantilevered grain bridging was 12.5 % at a test temperature of 800°C. For room temperature testing, this proportionality constant was 23 %. The lesser number of elastic and cantilever grain bridging at elevated temperature is indicative of the increase in grain boundary sliding.

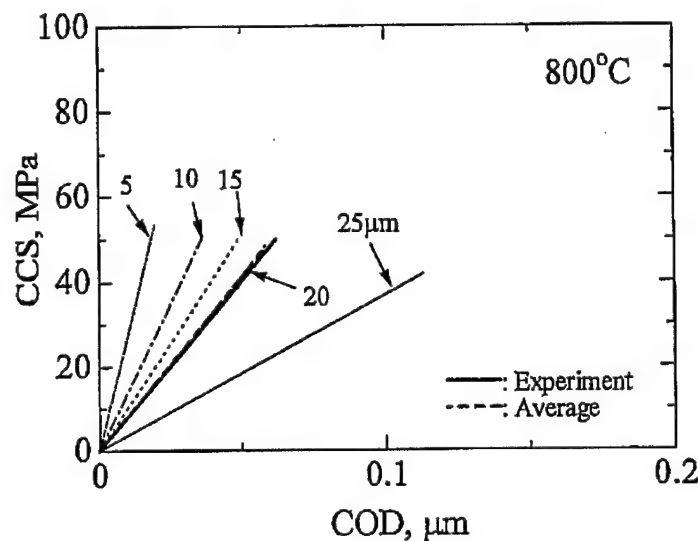


Fig. 1.6. CCS versus COD relations at 800°C.

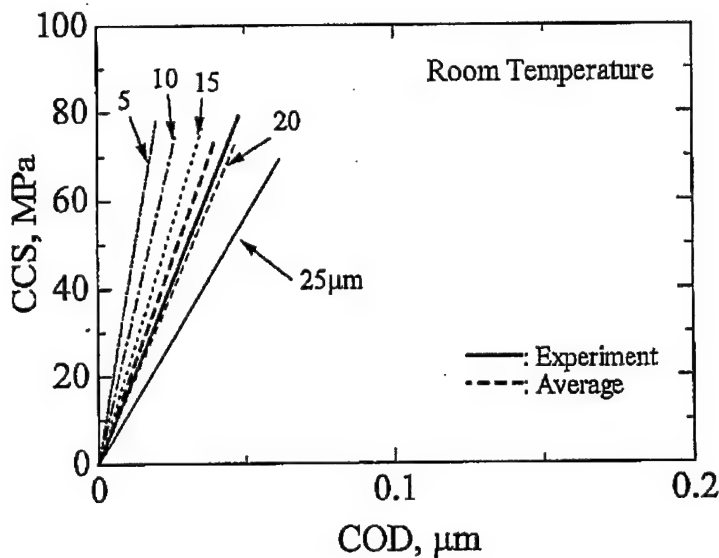


Fig. 1.7. CCS versus COD relations at room temperature

In the absence of any micro-mechanical data, the friction coefficient for estimating the resistance to the subsequent intergranular sliding was assumed to be 0.7. The Coulomb friction coefficient was an educated average of the bulk friction coefficients given by Jahanmir and Dong [10] and was adjusted to account for the rougher surfaces due to the presence of the interstitial phase.

1.3 Results

Initially, the FE model was subjected to a cool down process from 1500°C to 20°C or 800°C. The model was then subjected to cyclic loading. The relative contributions of the various bridging mechanisms to the CCS were adjusted to match the CCS versus COD relation. The computed and measured unloading CCS vs. COD relations at locations 0.1, 1.0 and 2.0 mm from the crack tip are also shown in Figures 1.8 and 1.9. In all cases, the COD did not return to zero. These results show that additional compressive force is required to return the grains to their original un-cracked position. Furthermore, the good agreement of the FE results and the experimental data indicates that the assumptions and modeling techniques used were successful in representing the micro-mechanics of grain bridging in alumina during loading and unloading.

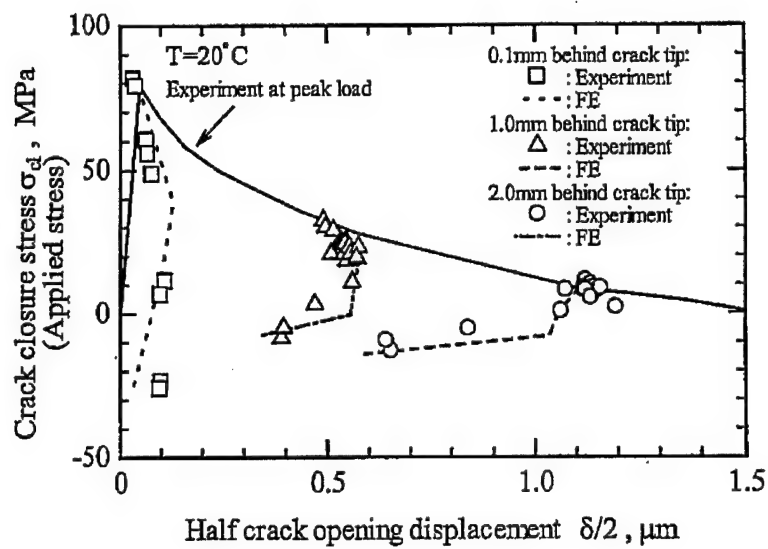


Fig. 1.8. CCS vs. COD relations during the first loading and unloading at room temperature.

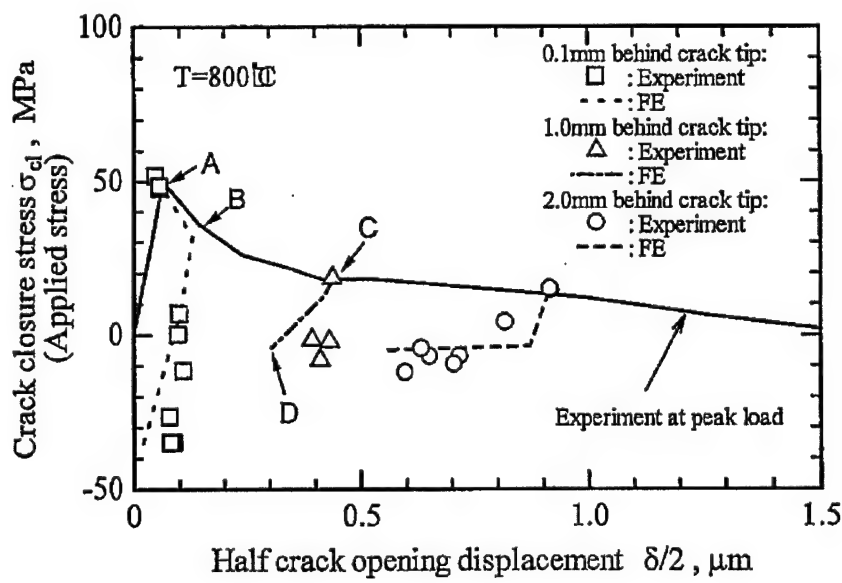


Fig. 1.9. CCS vs. COD relations during the first loading and unloading at 800° C.

Figure 1.10 shows the localized concentrations of the von Mises stress at the elastic grain bridges and the angled, frictional interfaces at A, B, C and D on the CCS versus $\delta/2$ curve of Figure 1.9. The highly concentrated Mises stresses are generated around both of the angled interface and the elastic element. On the other hand, the frictional interfaces do not generate a large stress.

Figures 1.11 and 1.12 show the variations in CCS with grain size and location from the crack tip at 800° C and room temperature, respectively.. The CCS of the smaller grains, i.e. 5 and 10 μm , which are largest at the crack tip, are larger than the CCS of the larger grains of 15 ~ 25 μm .

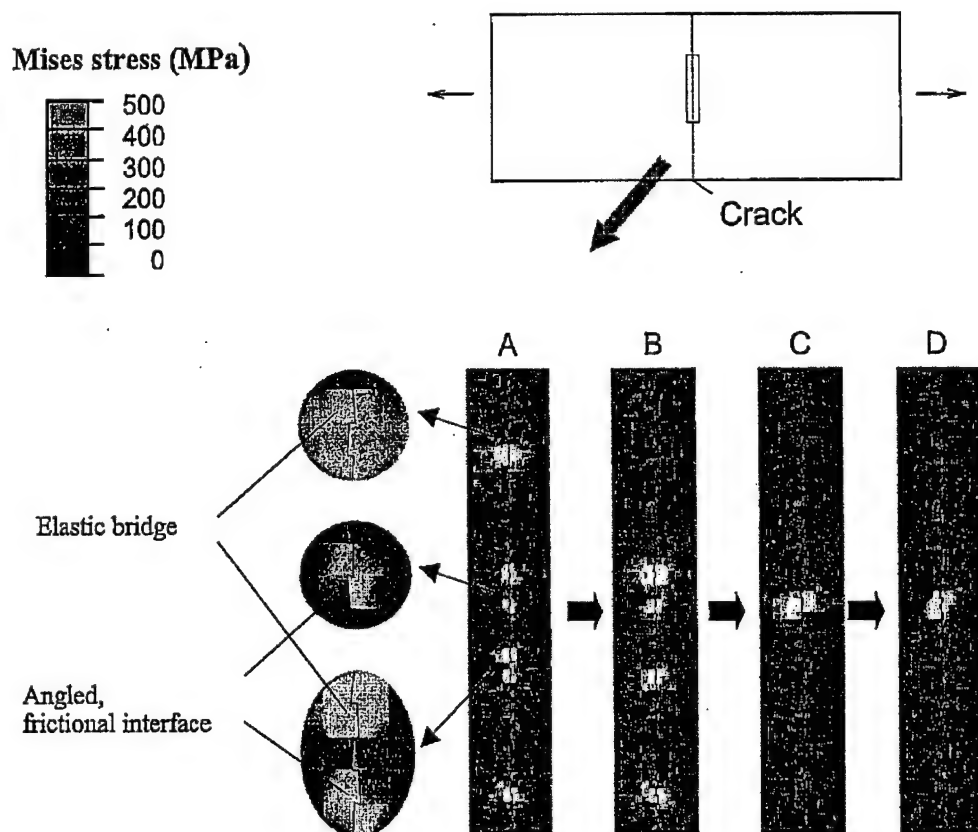


Fig. 1.10. Variation of Mises stress distribution along the crack at maximum load.
($T = 800^\circ\text{C}$, grain size=15 μm)

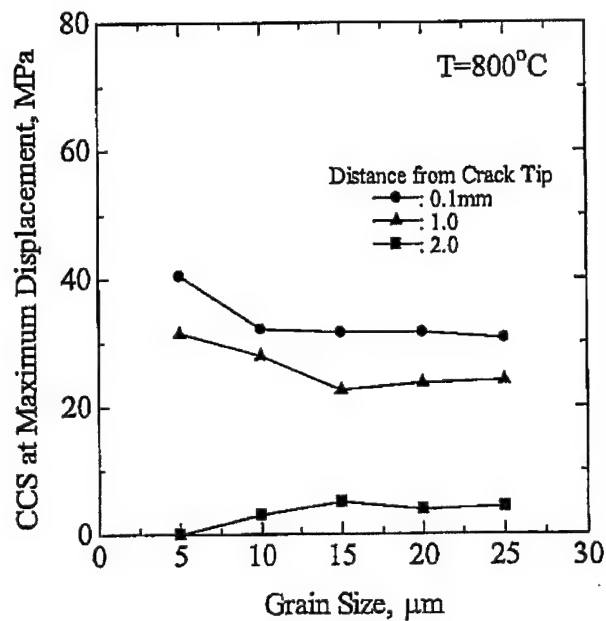


Fig. 1.11. Variation in CCS at maximum applied displacement at 800°C .

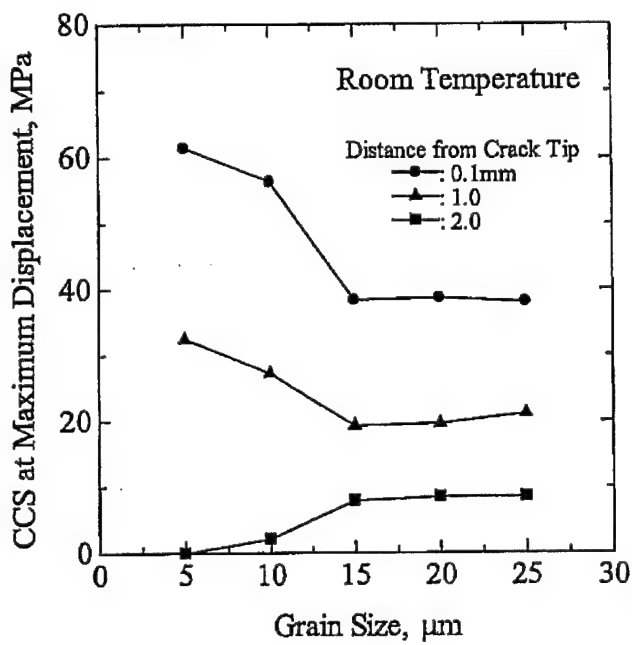


Fig. 1.12 Variation in CCS at maximum applied displacement at room temperature.

Finally, the crack closing stress intensity factors at room temperature and 800°C due to crack closure forces along the FPZ are shown in Figure 1.13. If the alumina WL-DCB specimen was composed entirely of 5 μm grains, the stress intensity factors at peak load and at room temperature and 800°C would have been 3.4 MPa $\sqrt{\text{m}}$ and 2.81 MPa $\sqrt{\text{m}}$, respectively. The integrated sum of the crack closure stress intensity factors for alumina WL-DCB specimen with grain size distribution of Figure 1.3 were 2.73 MPa $\sqrt{\text{m}}$ and 2.36 MPa $\sqrt{\text{m}}$ at room temperature and 800°C, respectively.

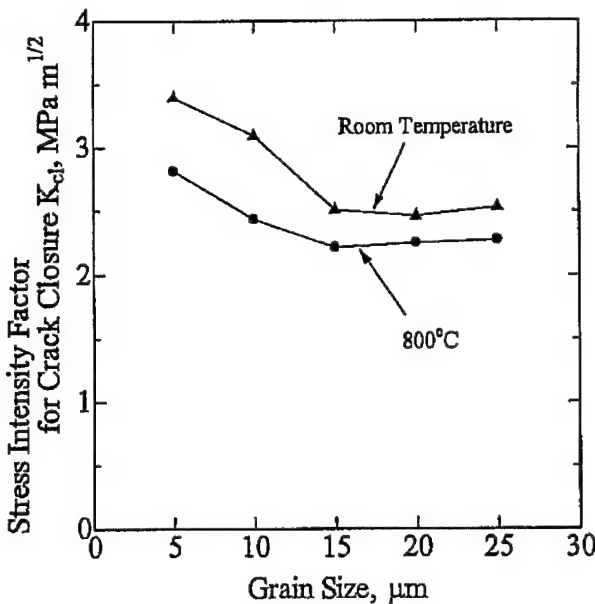


Fig. 1.13 Crack closure stress intensity factor for each grain size.

1.4 Conclusion

A micro-mechanical FE model, which is based on grain pullout and push-in is presented. The FE model, which was developed through a hybrid experimental-numerical, inverse process, successfully replicated the measured cyclic load and unload relations of an alumina WL-DCB specimen.

Optimization study based on the crack bridging forces showed that Al_2O_3 with all 5 μm grain provided the largest K_{IC} of 3.4 MPa $\sqrt{\text{m}}$ and 2.81 MPa $\sqrt{\text{m}}$ at room temperature and 800°C, respectively.

CHAPTER 2 A FE MODEL OF CARBON/CARBON COMPOSITE FRACTURE

2.1 Hybrid Moiré-FE Analysis

2.1.1 Single-edged Notch Bend (SENB) Specimen

The fracture specimen used in this proof-of-concept study is a 2-D, carbon-fiber reinforced carbon matrix (C/C) composite, single-edged notch bend (SENB) specimen with a straight notch in the T-S plane of a C/C plate. This relatively porous composite is a 12.7 mm thick plate of stacked plies of discontinuous carbon fibers impregnated with a carbon matrix as shown in Figure 2.1. Its bulk density is 1.54 gr/cc with a porosity of 16%, compressive strength of 200 MPa and a fiber volume fraction of 40%.

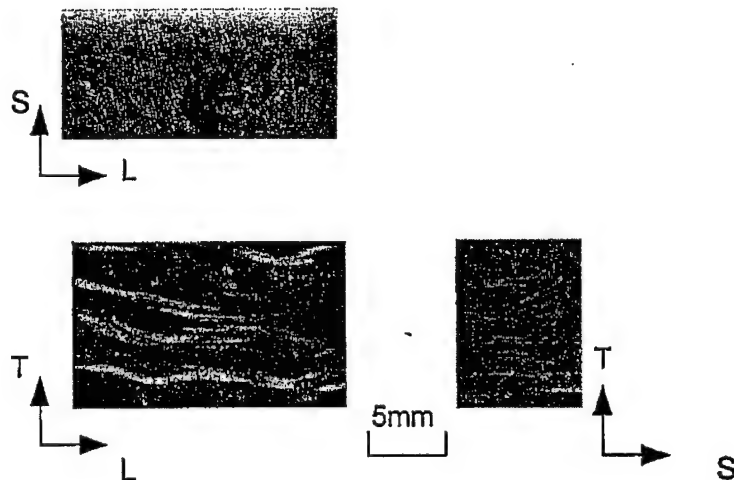


Fig. 2.1. C/C composite.

Figure 2.2 shows the SENB specimen with a 50% side groove. The support span for the three-point bend fixture was 48 mm. Uniaxial tension tests in the L-T and T-L directions yielded a relatively uniform elastic modulus of $E_T/E_L = 48$ GPa. Two of the three remaining elastic modulus of $E_S = 0.67$ GPa and the shear modulus of $G_{LS} = 1.92$ GPa were obtained through an inverse analysis, which is discussed later, by matching the response of a FE model of the SENB specimen with the experimentally obtained load versus load-line displacement and the load versus crack mouth opening displacement (CMOD) relations. A Poisson's ratio of $\nu = 0.05$ was obtained from Ohtake et al [11].

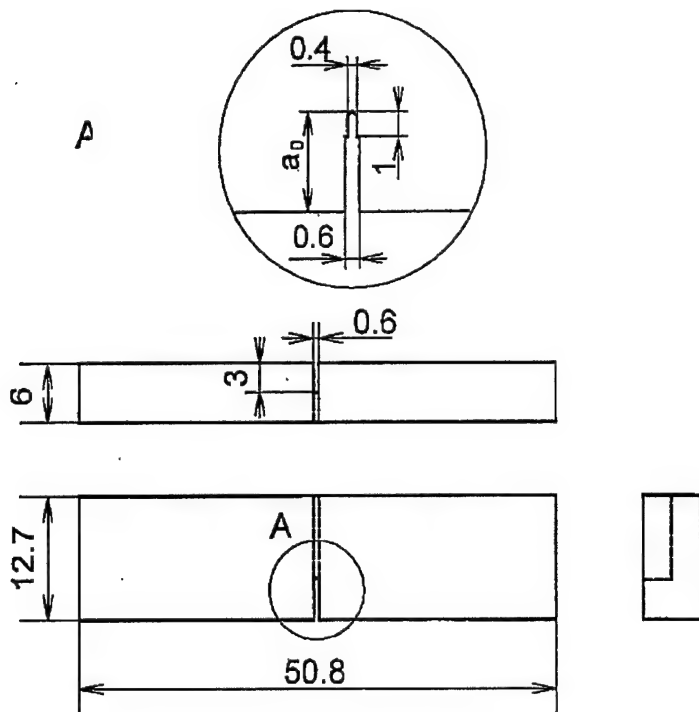


Fig. 2.2. C/C composite SENB specimen.

2.1.2 Three-point Bend Test

The C/C composite SENB specimen was subjected to a three point bend test. As illustrated in Figure 2.3, the crack propagated in an irregular zig-zaged pattern along the side groove and fractured in a likewise pattern. The corresponding load versus load-line displacement curve is shown in Figure 2.4 where Pt. A is the onset of crack growth. Extensive crack growth occurred with the maximum load at Pt. B and complete penetration of the crack through the height of the SENB specimen occurred at Pt. C. The extensive crack bridging kept the two specimen halves together through an applied load line displacement of 2 mm.

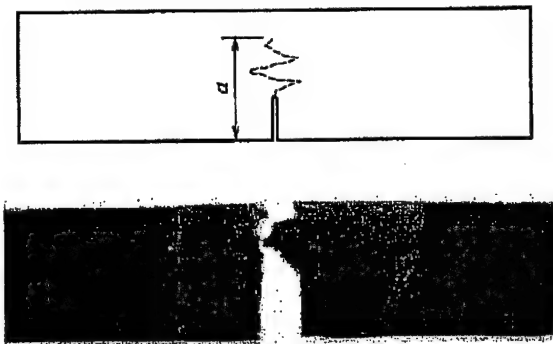


Fig. 2.3. Crack path and fractured C/C SENB specimen.

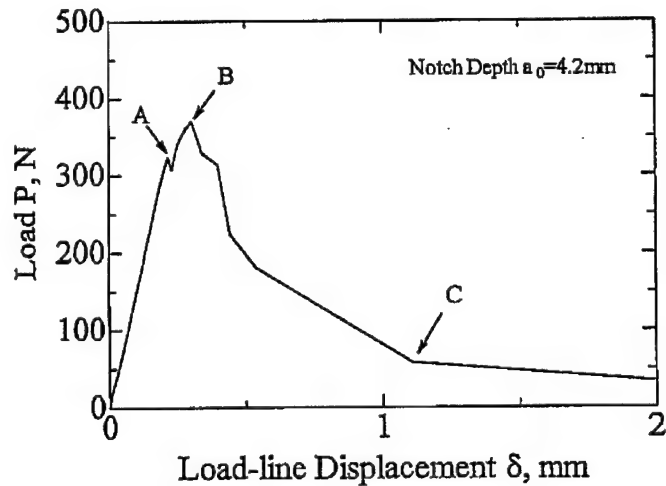


Fig. 2.4. Load versus load-line displacement with crack growth.
C/C SENB specimen.

The area under the load versus load-line displacement in Figure 2.4, for a given applied load line displacement, is the work of fracture. The difference in the work of fracture with an incremental increase in crack length is the work rate of fracture.

In order to assess the effect of crack bridging generated by the zig-zagged crack path, the stress intensity factor of a postulated self-similarly extended crack was calculated for various machined notch lengths, a_0 , as shown in Figure 2.5, using the standard LEFM formula [12] of:

$$K_I = \frac{PS}{BW^{\frac{3}{2}}} \frac{3\left(\frac{a}{W}\right)^{\frac{1}{2}} \left[1.99 - \frac{a}{W} \left(1 - \frac{a}{W}\right) \left(2.15 - 3.93 \frac{a}{W} + 2.7 \frac{a^2}{W^2} \right) \right]}{2\left(1 + 2\frac{a}{W}\right)\left(1 - \frac{a}{W}\right)^{\frac{3}{2}}} \quad (2.1)$$

Region A in Figure 2.5 shows that for the same total crack length, a shorter initial notch required a higher stress intensity factor for crack growth due to the longer FPZ which provided a larger crack bridging (closing) force. In Region B with a longer total crack length, this difference disappeared as the crack grew with a constant FPZ size. The increase in resistance to crack growth is shown by Figure 2.6, which plots the initiation stress intensity factor at the onset of crack growth from the machined notch tip and the stress intensity factor at maximum load in terms of an increasing notch depth.

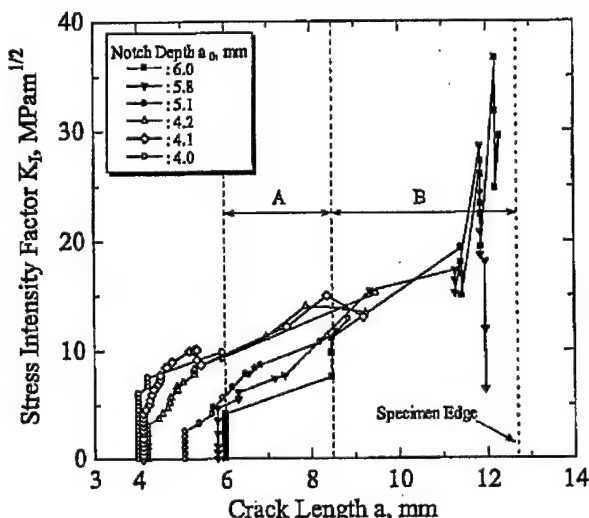


Fig. 2.5. Stress intensity factor of a straight crack in a C/C SENB specimen.

2.1.3. Re-notching Test

The crack bridging stress (CBS) acting along the FPZ of a postulated self-similarly crack extension was determined by re-notching the SENB specimen. The incrementally re-notched SENB specimen was then re-loaded back to its maximum load and the load versus load-line displacement relation shown by Figure 2.7 was obtained. The residual load-line displacement at complete unloading in this figure is attributed to the resistance of the pulled out fibers to crack closure. The area under the loading curve provided the work of fracture. The specimen compliance increased with increasing re-notch length with a total crack length of 9.25 mm.

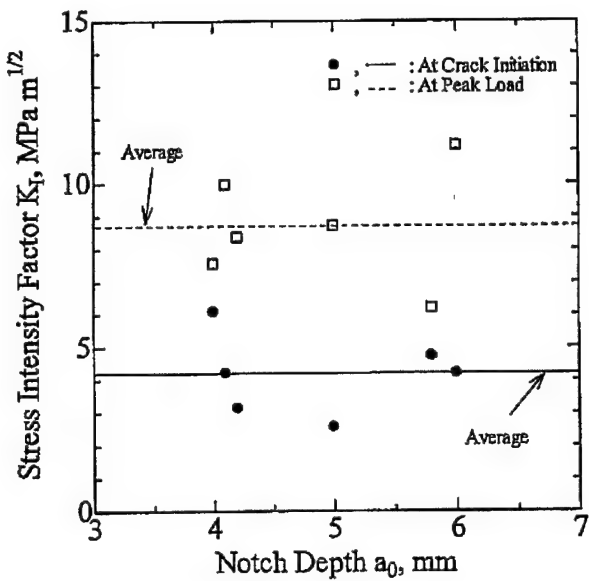


Fig. 2.6. Stress intensity factor at crack growth initiation and maximum load.

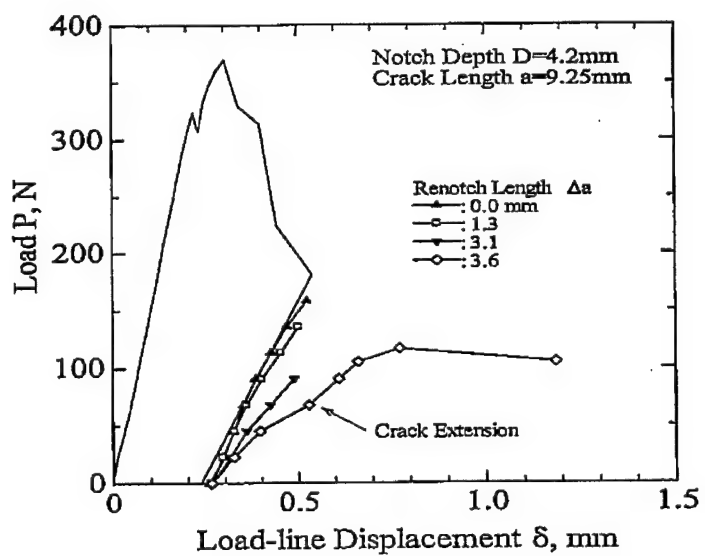


Fig. 2.7. Load versus load-line displacement relation of re-notched C/C SENB specimen.

2.1.4. Moiré Interferometry

The crack opening profile and the lateral displacement field during the re-notching test were determined by moiré interferometry. The moiré interferometer was configured to yield an effective grating frequency of 1,200 lines/mm for an actual grating frequency of 600 lines/mm. Figure 2.8 shows moiré interferometer setup which was used in this room temperature test. The Moiré fringe pattern was recorded at the maximum load of each re-notching process. Figure 2.9 shows the actual zig-zagged FPZ and the moiré pattern surrounding this FPZ. The moiré data was used to determine the COD along the original machined notch and the re-notched crack as an input to the FE analysis.

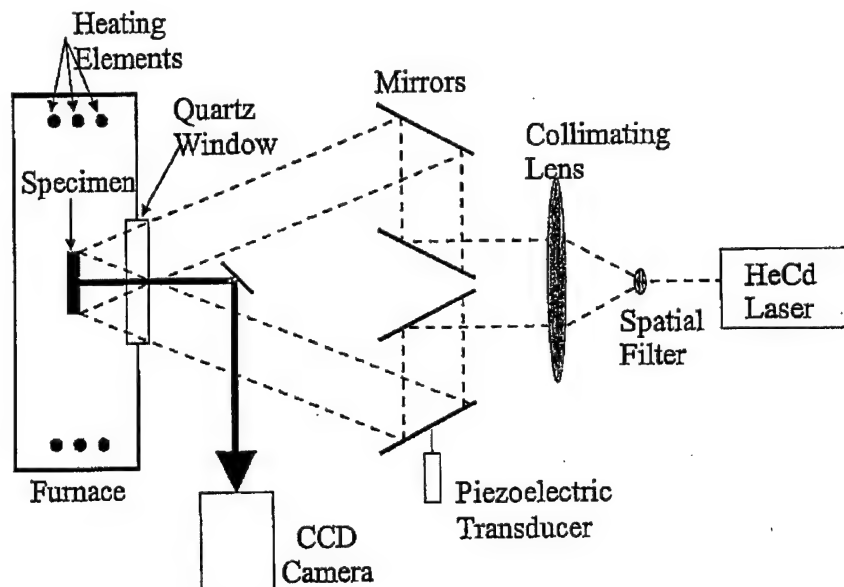


Fig.2.8. High temperature moiré interferometry setup.

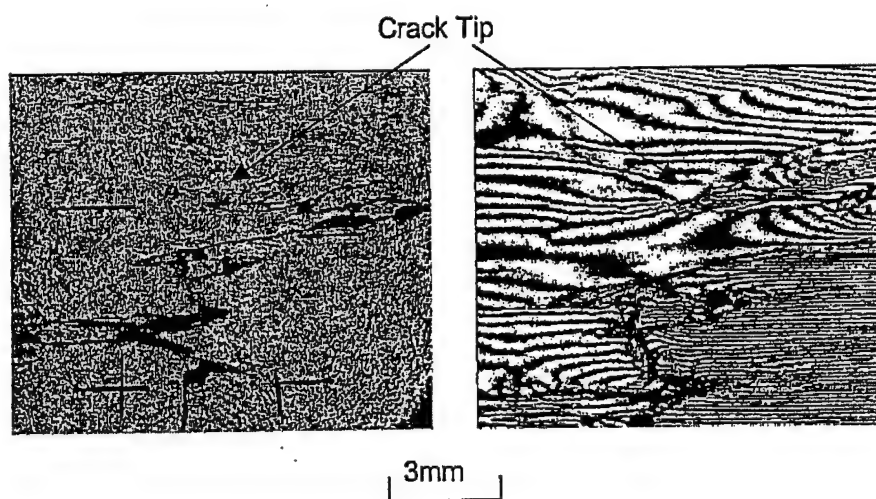


Fig. 2.9. Actual FPZ and moiré pattern.

2.1.5. Finite Element Modeling

A FE model of the SENB specimen with a straight FPZ was used to compute, through an inverse analysis, the CBS acting on the FPZ. Figure 2.10 shows the FE mesh which models one half of the SENB specimen. The FE analysis consisted of matching the computed and moiré COD's, through an inverse iterative process, for an assumed CBS distribution at various re-notched lengths. The final FE analysis yielded the effective stress intensity factor for the C/C SENB specimen with an idealized crack bridging stress.

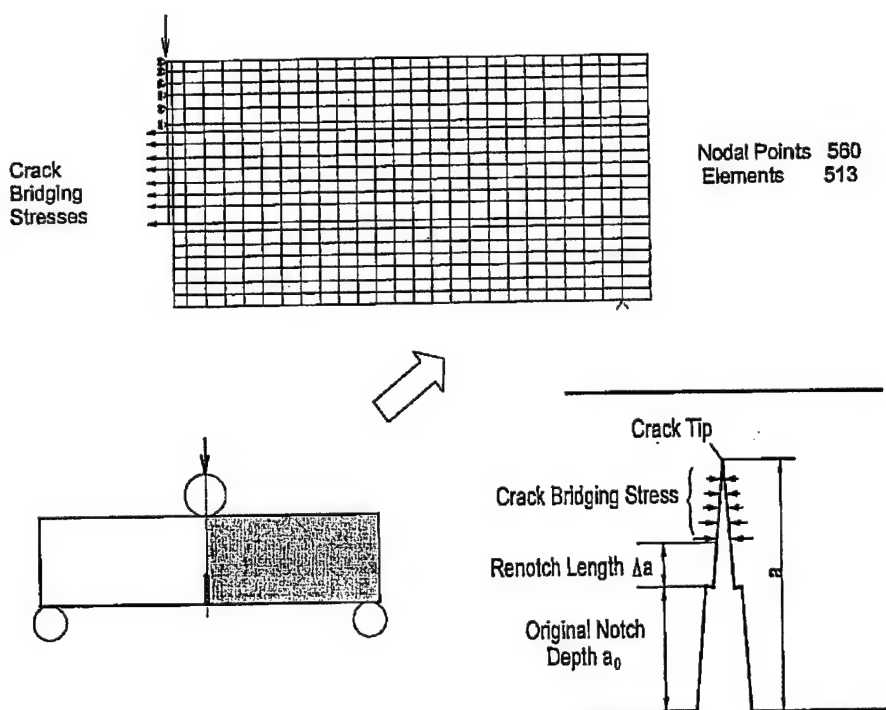


Fig. 2.10. FE model of the re-notched C/C SENB specimen.

2.2. Results

The crack was grown to a straight crack length of 9.25 mm or 5.05 mm from the machined notch tip. This growth, Δa , as shown in Figure 2.10, is defined as the projected length of the zig-zagged crack path. Figure 2.11 shows the COD variation with re-notching. The area under the load versus load line displacement curve, which is the work of fracture, was then obtained.

Figure 2.12 shows the change in the crack bridging stresses with re-notching in the frontal FPZ. The bridging stress is largest at the machined notch tip, i.e. the location of maximum fiber pull out. The FE analysis then computed the reduction in stress intensity factor due to fiber bridging, K_c , from which the following equivalent stress intensity factor, K_{eq} , was obtained:

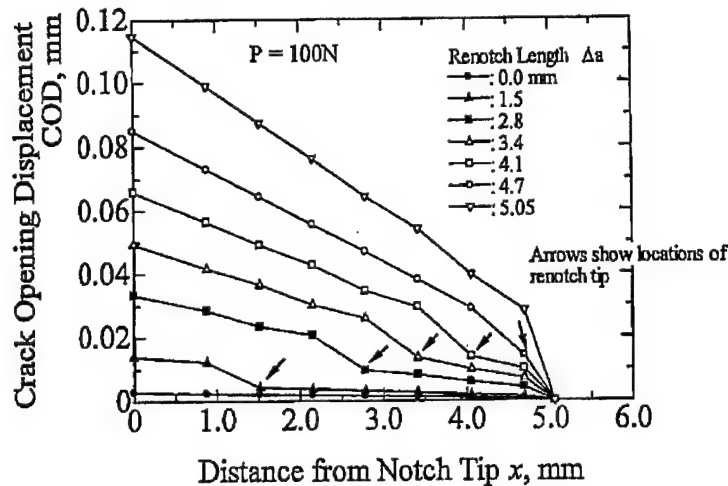


Fig. 2.11. COD profiles.

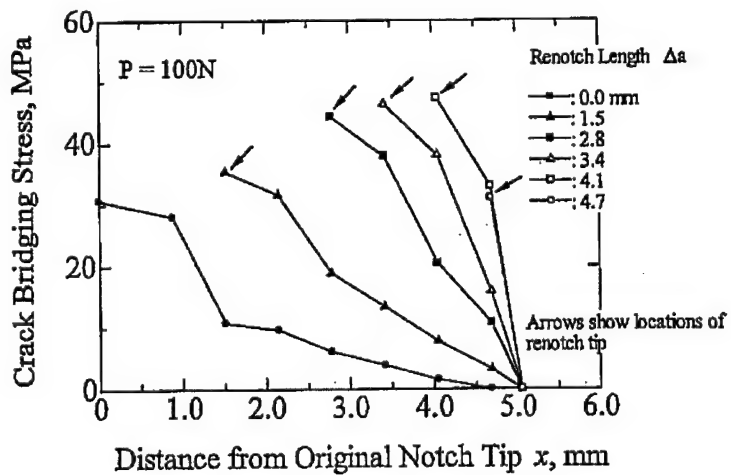


Fig. 2.12. Crack bridging stress.

$$K_{eq} = K_I - K_c \quad (2.2)$$

$$G_{eq} = G_I - G_c \quad (2.3)$$

$$G_{eq} = \frac{K_{eq}^2}{E} \quad G_I = \frac{K_I^2}{E} \quad (2.4)$$

where the G 's are the corresponding energy release rates. From Eqs. (1)-(3),

$$\frac{K_{eq}}{K_I} = \sqrt{\frac{G_{eq}}{G_I}} = \sqrt{1 - \frac{G_c}{G_I}} \quad (2.5)$$

$$\frac{K_c}{K_I} = 1 - \frac{K_{eq}}{K_I} = 1 - \sqrt{\frac{G_{eq}}{G_I}} = 1 - \sqrt{1 - \frac{G_c}{G_I}} \quad (2.6)$$

Figure 2.13 shows the computed reduction in stress intensity factor with the increase in re-notch length due to the crack bridging stress.

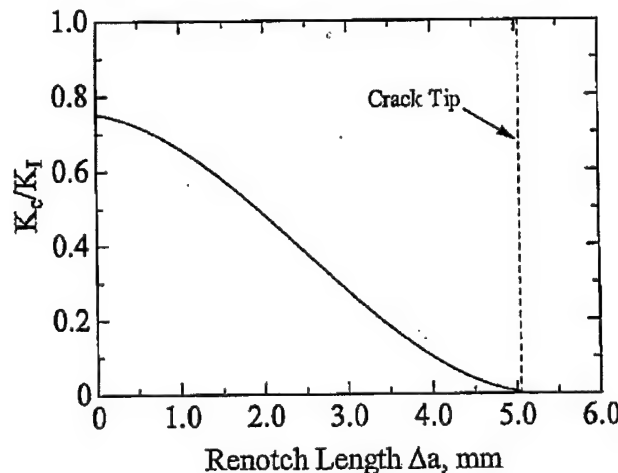


Fig. 2.13. Reduction in bridging stress intensity factor.

Figure 2.14 shows that the measured work rate of fracture, G_I , is closely related to the computed stress intensity factor of the SENB specimen with crack bridging. The stress intensity factor is normalized by the modulus for an equivalent isotropic material, E_c , of:

$$\frac{1}{E_c} = \sqrt{\frac{A_{11}A_{22}}{2}} \left[\sqrt{\frac{A_{22}}{A_{11}}} + \frac{2A_{12} + A_{66}}{2A_{11}} \right]^{\frac{1}{2}} \quad (2.7)$$

$$\begin{aligned}
 A_{11} &= 1/E_y = 1/0.67 \\
 A_{22} &= 1/E_x = 1/48.0 \\
 A_{12} &= -v/E_x = -0.05/48.0 \\
 A_{66} &= 1/G_{xy} = 1/1.92
 \end{aligned}$$

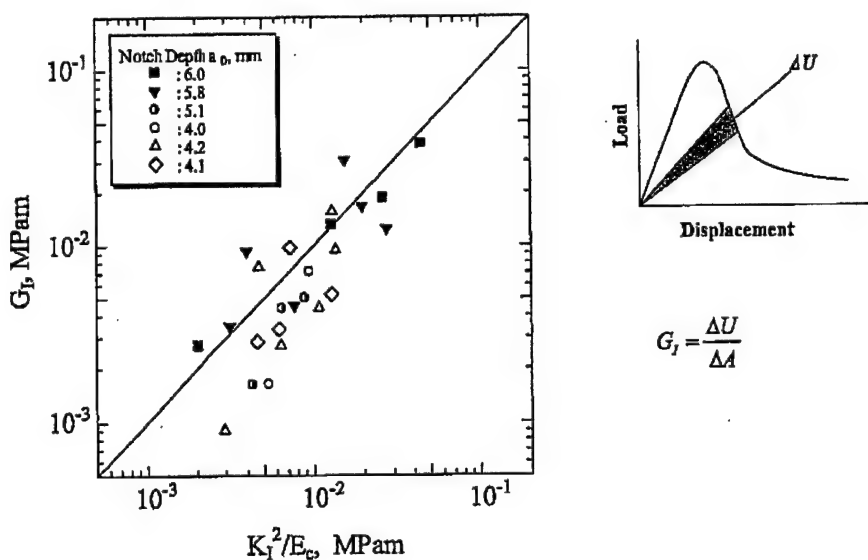


Fig. 2.14. G_I versus K_I .

Since Figure 2.14 implies that $U \propto G$

$$\frac{K_c}{K_I} \approx 1 - \sqrt{1 - \frac{U_c}{U_I}} \quad (2.8)$$

which simplifies the computation of K_c .

2.3. Conclusions

A hybrid experimental-numerical, inverse procedure was used to model the crack bridging stress of the tortuous crack in a C/C composite SENB specimen.

The measured work rate of fracture was found to be nearly equal to the strain energy release rate obtained from the stress intensity factor of a carbon/carbon composite SENB specimen.

CHAPTER 3 CRACK BRIDGING FORCE IN MULLITE/ALUMINA COMPOSITE

3.1 All Oxide Composite

The ceramic fiber-ceramic matrix considered here is an all-oxide continuous fiber ceramic composite (CFCC) which in principle is immune to oxidation, less sensitive to moisture attack and thus is a viable CFCC for long term, high temperature applications. The oxide fiber used in this study is a Nextel 720 fiber cloth (8 harness satin weave) with a matrix of 80 percent mullite and 20 percent alumina. The CFCC plate consists of twelve plies of 0°/90° laminates with a total thickness of 3.35 mm. The matrix porosity increases the damage tolerance of the overall composite while decreasing the matrix strength and the matrix toughness [13]. Matrix porosity also decreases the inter-laminar shear strength and the notch sensitivity of the CFCC material [13 - 17]. The low interlaminar shear strength, in particular, resulted in delamination at a low compressive load and triggered a lengthy quest of developing a suitable fracture specimen.

3.2. Experimental Procedure

The two all-oxide CFCC plates considered in this study were identical in composition but were fabricated with two or four cycles of precursor impregnation and pyrolysis resulting in different fracture responses. These two CFCC plates are identified as CFCC-A (35.5% porosity) and CFCC-B (31% porosity), respectively.

3.2.1 SEN Specimen

The wedge-loaded double cantilever beam (WL-DCB) fracture specimen, which was used in the past fracture analysis of dense monolithic ceramics [3-6], was ineffective due to the weak interlaminar shear and compressive strength of the all-oxide CFCC plate tested. Either the loading points on the WL-DCB specimen collapsed or the specimen delaminated prior to crack extension. Thus a single edge notch (SEN) specimen, as shown in Figure 3.1, clamped between two large grips was used to avoid delamination and compression failure at the load points of the specimen. Since the purpose of this study was to develop a phenomenological model of the FPZ associated with the CFCC fracture specimen in toto, no side grooves were machined on the specimen. The crack was machined with a 0.4 mm blade and the machined notch tip was chiseled with a razor blade so that the starter crack resembled an ideal crack tip. The SEN specimen was then loaded in a displacement controlled, simple tension fixture and the crack opening profile was recorded. The crack mouth opening displacement (CMOD) was also recorded with a clip gage.

3.2.2. Fracture Test

Initial attempts to record the crack opening profile by moiré interferometry of the CFCC-A SEN specimen failed as the specimen warped under load. Thus, the crack opening profiles on both sides of the SEN specimen were obtained from the CCD images of the fracturing SEN specimens. This recording was enhanced by painting the specimen surfaces black to contrast the specimen surface with the exposed white fiber tows. Figure 3.2 shows the gripped SEN (CFCC-B) specimen, which had fractured, with the crack mouth opening displacement (CMOD) gage attached. Figure 3.3 shows the back side of this fracture specimen. The complex crack profile is due to the 0° ply, which failed in shear, facing this back surface. This discontinuous fracture surface with 90° and 0° fiber pull outs is also documented in [16] and is attributed to the efficacy of the porous matrix as a crack deflection mechanism within and between the fiber tows.

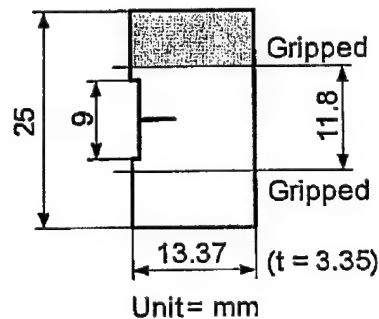


Fig. 3.1. SEN specimen.

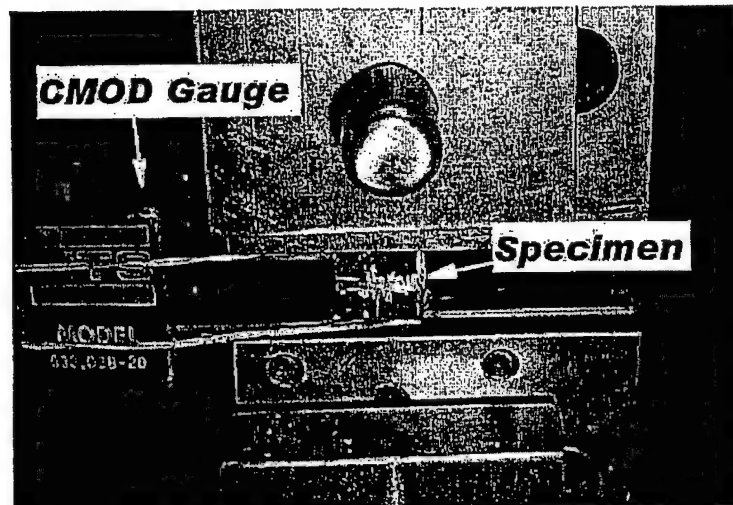


Fig. 3.2. Fractured SEN specimen with CMOD gage attached.



Fig. 3.3. Photo of fractured specimen.
Back side of a CFCC-B SEN specimen.

Figures 3.4 and 3.5 show close up views of fiber pull outs in the 90° (parallel to the load) and 0° (parallel to the crack) directions. While the pull out of the fiber tows in the 90° direction dominate, 0° fiber pull out and fiber breakage in the 0° tows were inevitable for the crack to propagate in the 0° direction.

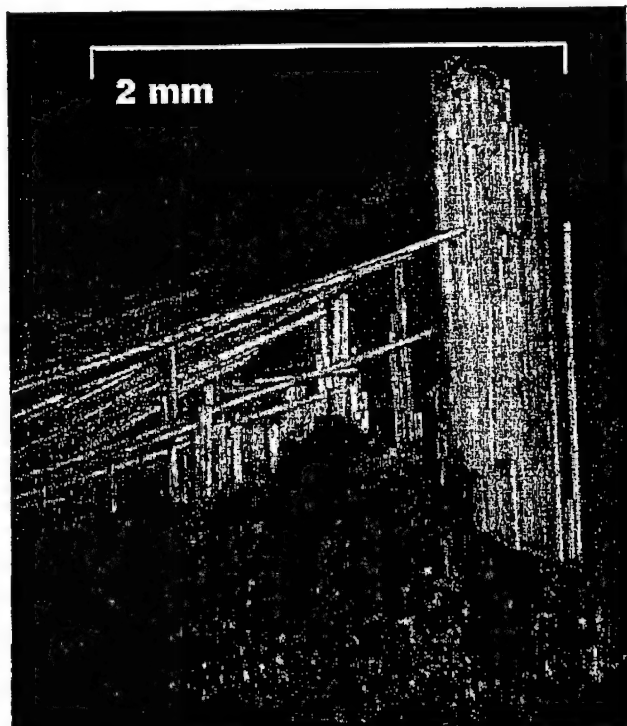


Fig. 3.4. Fiber pullout I. CFCC-B specimen.

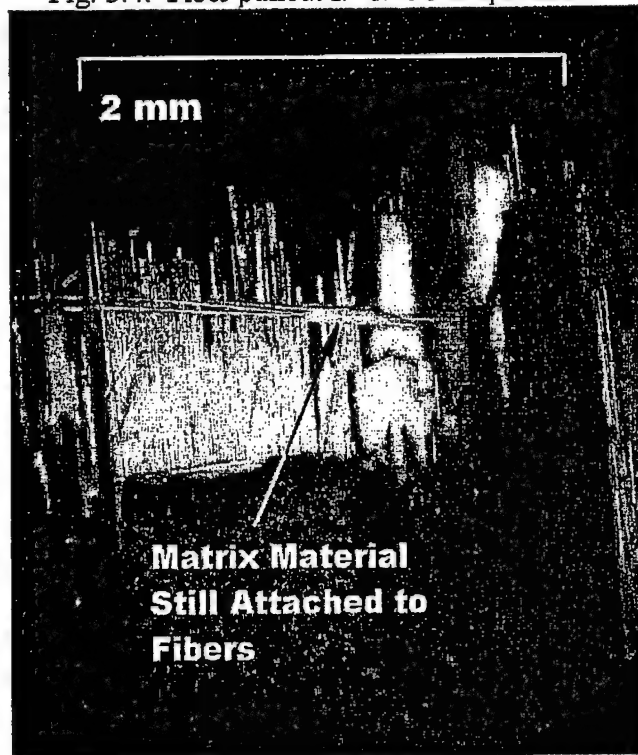


Fig. 3.5. Fiber pullout II. CFCC-B specimen.

At peak load, a large crack jump with rapid unloading in the CFCC-A specimens was followed by approximately 3 mm of intermittent stable crack extension, as shown in Figure 3.6. Load and crack mouth opening displacement (CMOD) were recorded

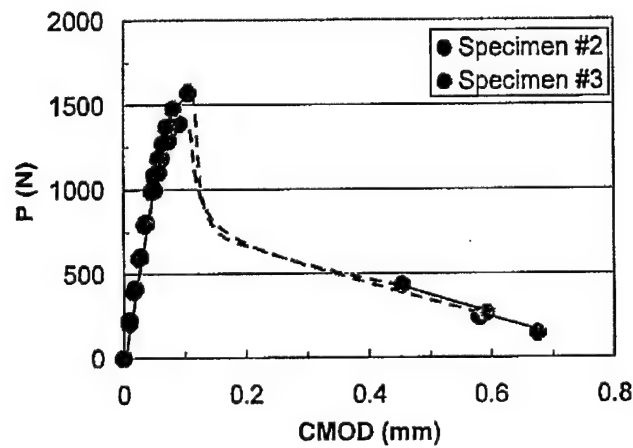
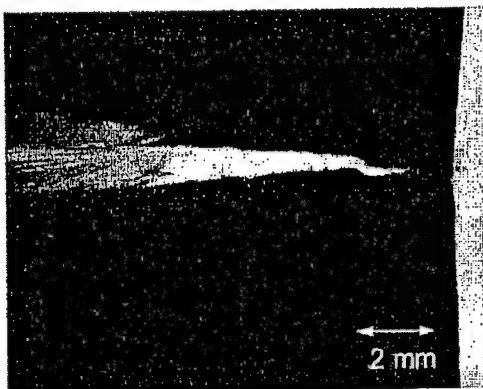


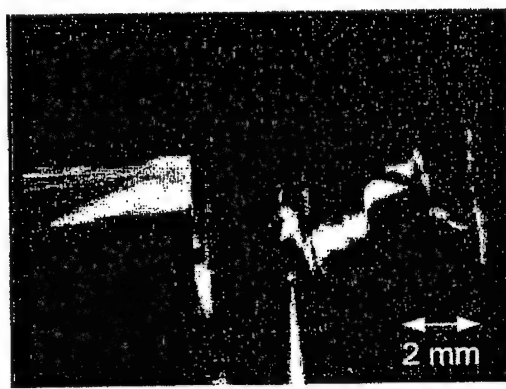
Fig. 3.6. Load versus CMOD. CFCC-A SEN specimen

under monotonic loading.

throughout this stable crack growth process. This process was repeated for three specimens to obtain crack opening profiles at several levels of crack extension. The significant difference in the crack opening profiles of the front and back surfaces, as shown in Figure 3.7 required educated judgment in order to derive a smoothed crack opening profile compatible with the observed jagged COD profiles.



Front surface



Back surface

Fig. 3.7. Crack opening profile of CFCC-A SEN specimen.

Moiré interferometry was used to determine the crack opening profile in the more brittle CFCC-B SEN specimens. A total of three specimens were loaded monotonically, as shown in Figure 3.8, and analyzed with moiré interferometry. A photograph of the moiré interferometry bench is shown in Figure 3.9. This set up is essentially same as that shown schematically in Figure 2.8 except for the two input beams, which are in a vertical plane for vertical displacement measurement, as shown in Figure 3.10. Figure 3.11 shows a typical moiré fringe pattern.

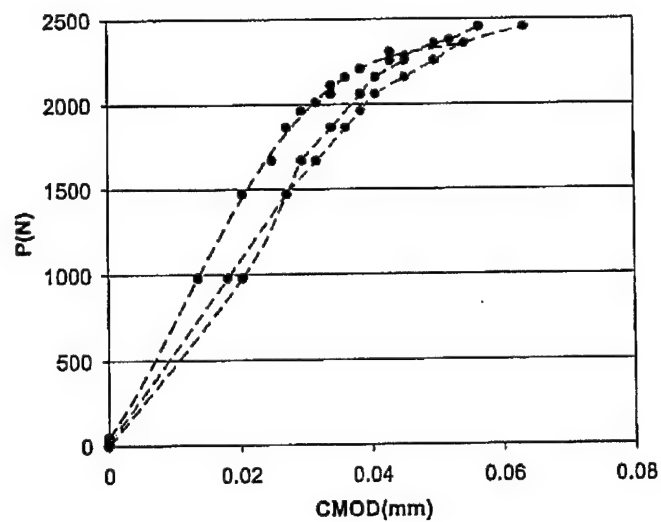


Fig. 3.8. Load versus CMOD of monotonic loaded CFCC-B SEN specimen.

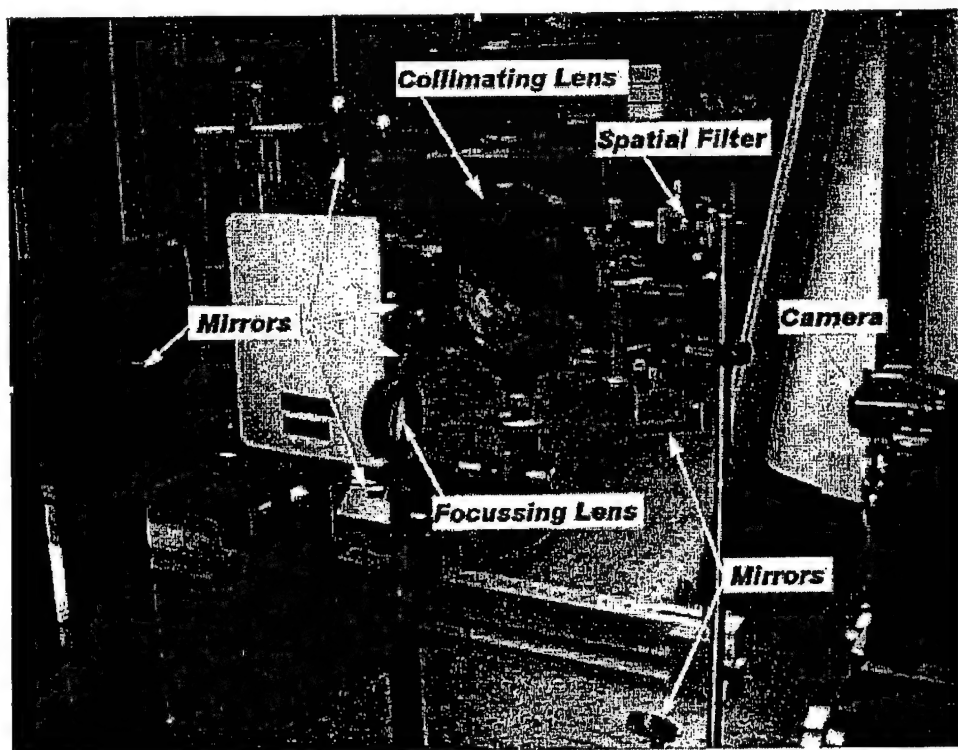


Fig. 3.9. Moiré interferometry bench.

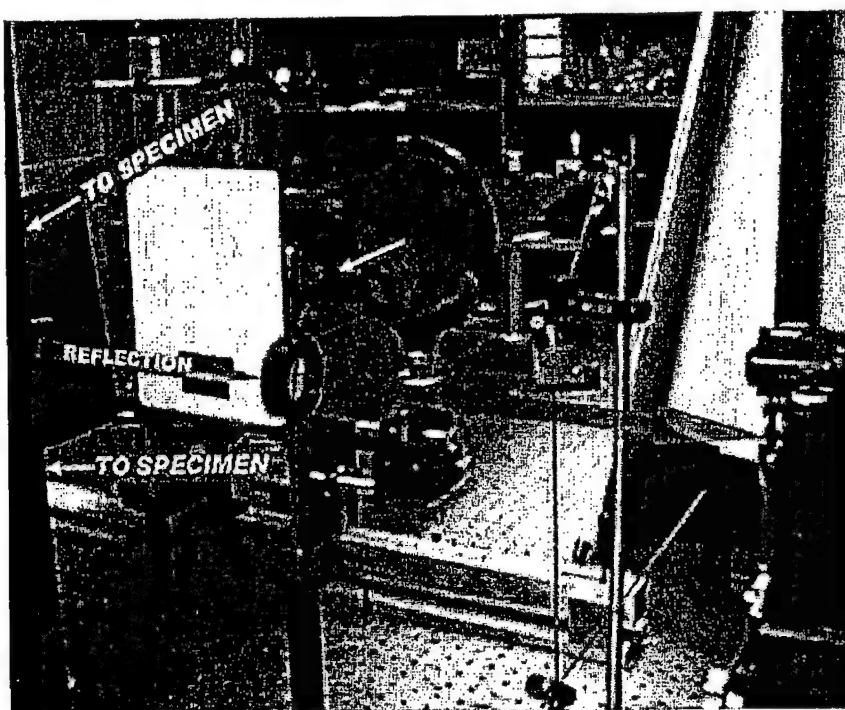


Fig. 3.10. Moiré interferometry bench with light beams marked.

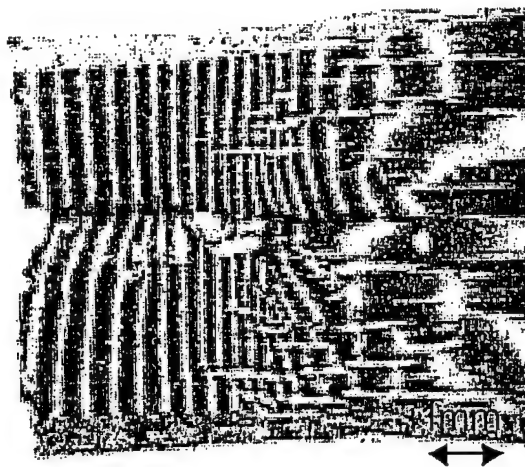


Fig. 3.11. Moiré interferometry image.
Front side of CFCC-B SEN specimen.

Also two specimens were cyclic loaded and the corresponding FPZ's at two loads, including the unloaded point, were analyzed. Figure 3.12 shows the load versus CMOD and a moiré interferometry photo of a cyclic loaded CFCC-B SEN specimen. The crack

bridging stress versus COD relations were determined at the locations where the moiré pictures were taken.

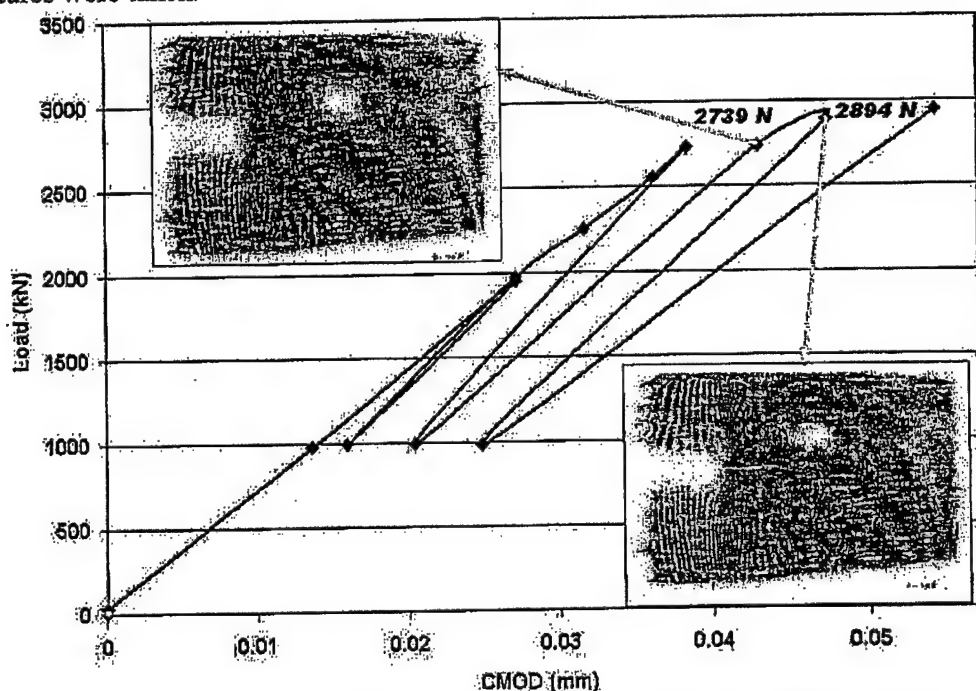


Fig. 3.12. Load versus CMOD of a cyclic loaded CFCC-B SEN specimen.

Figure 3.13 is a superposition of Figures 3.8 and 3.12 to show the increase in tensile strength due to cyclic loading.

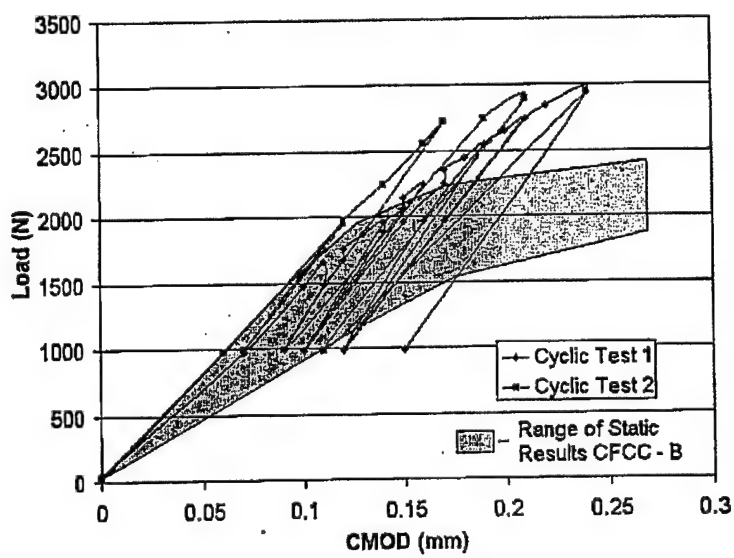


Fig.3.13. Load versus CMOD of monotonic and cyclic loaded

CFCC-B SEN specimens.

3.2. Numerical Model

Due to symmetry, only one half of the SEN specimen was modeled using 8 noded, isoparametric elements as shown in Figure 3.14. The crack tip singularity was roughly modeled by gradually reducing the size of the elements near the crack tip as shown in Figure 3.14b. The steel clamps were also incorporated in the FE model to replicate the complex loading condition of this short SEN specimen.

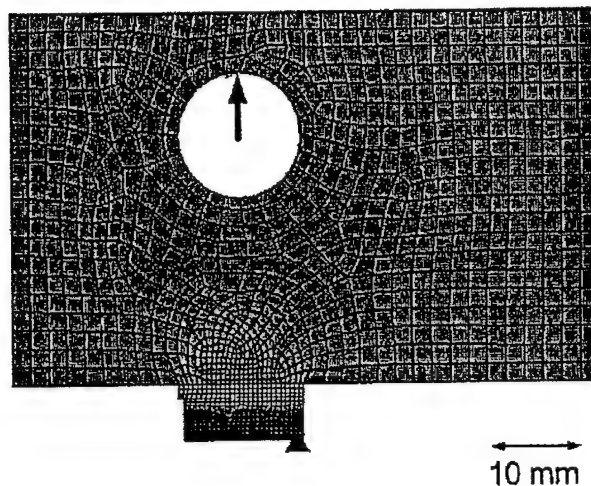


Fig. 3.14a. FE model of SEN specimen with clamped grips.

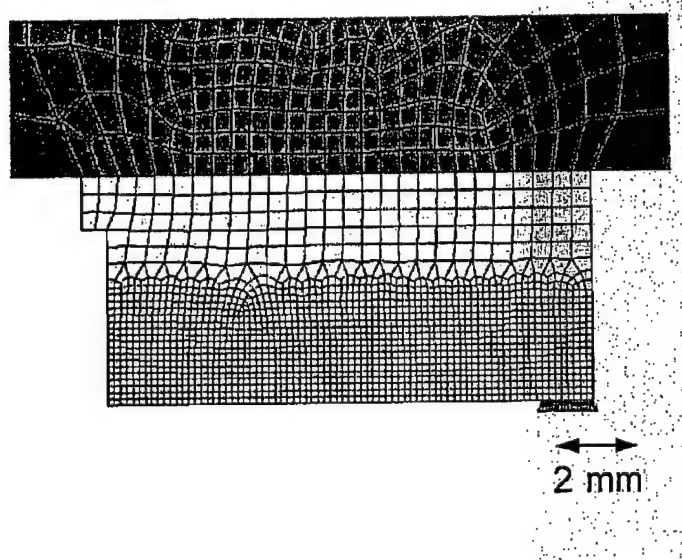


Fig. 3.14b. FE model of SEN specimen.

The orthotropic modulus of elasticity of this crossed ply, $0^\circ/90^\circ$, composite yielded different modulus of elasticity when a clip gag, which was used to measure the specimen extension, was mounted on the specimen surface with a 90° (front surface) or 0° (back surface) laminate. The modulus of elasticity, $E_x \approx E_y = 57.6$ GPa, is an average value of uniaxial tension tests in the longitudinal, 90° , and transverse, 0° , directions of the CFCC plate. The shear modulus, $G_{xy} = 7.23$ GPa was determined by the Iosipescu shear test as per ASTM D53791. Lacking any data, an assumed Poisson ratio of $\nu = 0.05$ [18] was used in the FE analysis.

3.3. Results

3.3.1. CFCC-A SEN specimen

Three CFCC-A SEN specimens, Nos. 1, 2 and 3, were tested and the crack opening profiles were determined through photographic recordings of the COD's. As mentioned previously, the crack propagated rapidly through two thirds of the specimen width at the peak load, after which stable crack growth was observed followed by a gradual decrease in load. The two specimen halves held together after the crack tip completely traversed the entire width of the specimen. Figure 3.15 shows the crack opening profiles for four crack growths which occurred past the maximum load in the descending portion of the load versus CMOD curves in Figure 3.6. Initially, the crack profile formed a parabolic crack opening, typical of a linear elastic fracture mechanic (LEFM) response, but this characteristic opening shape became obscure with the large opening and the rotation of the specimen halves.

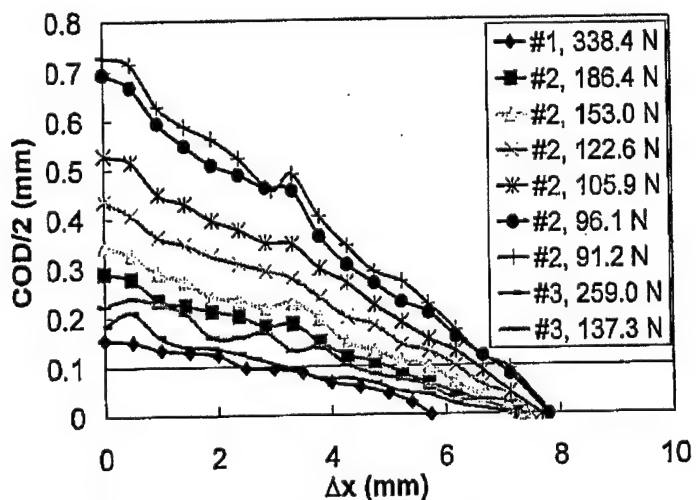


Fig. 3.15. Crack opening profile with crack extension.
CFCC-A SEN specimen under monotonic loading.

Figure 3.16 shows the crack bridging stress versus crack opening displacement (COD) with stable crack growth deduced using an inverse FE analysis with the COD of Figure 3.15. A comparison of the crack bridging force versus COD relation, which was obtained by the post fracture tension (PFT) method [19], with our results is more clearly shown in Figure 3.17.

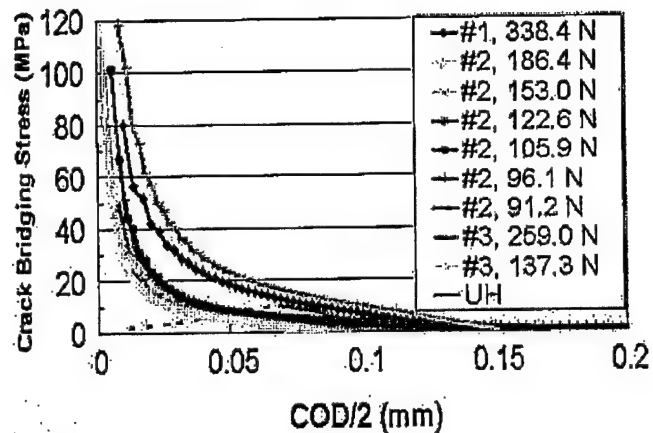


Fig. 3.16. Crack bridging stress versus COD relations of CFCC-A SEN specimen under monotonic loading.

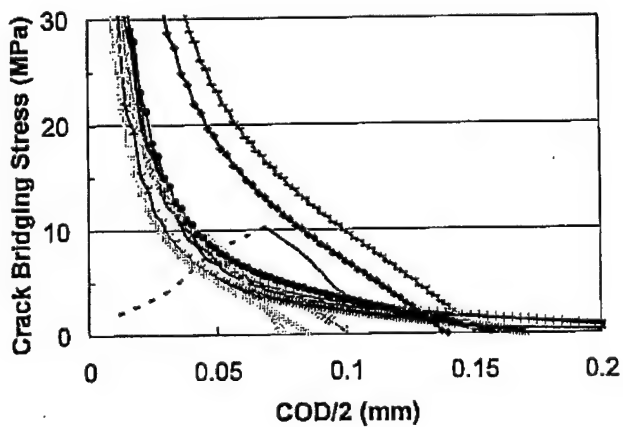


Fig.3.17. Enlarged section of Figure 3.16.
CFCC-A SEN specimen.

The CMOD data and the computed displacements of the clamped edge were then used to estimate the load-line displacement which was not measured but was computed by FE analysis in this study. The work of fracture, which is the area underneath the

resultant load versus the load line displacement curve was then determined. This work of fracture was 6820 J/m^2 .

3.3.2.CFCC-B SEN specimen.

As mentioned previously, this material, which had undergone four cycles of precursor impregnation and pyrolysis, was brittle and the crack propagated rapidly through the entire specimen width at the peak load without any subsequent stable crack growth as shown by the load versus CMOD curves of Figure 3.8. However, small stable crack growth was observed during monotonic loading, prior to the onset of fracture,

Figure 3.18 shows the final crack opening profile associated with a small crack extension in a monotonically loaded CFCC-B SEN specimen. Figure 3.19 shows the crack bridging stress versus crack opening displacement (COD) with stable crack growth deduced using an inverse FE analysis with the COD data of Figure 3.18. Note that the nearly constant crack bridging stress of about 90 MPa at a COD/2 of about 0.005 mm is in approximate agreement with the crack bridging force at the same COD/2 in Figure 3.16 of the CFCC-A specimen. Figure 3.20 shows the COD's measured by moiré interferometry and by those obtained by an inverse FE analysis. While better agreement with the measured COD's along the machine surface notch was desired, the agreement between the measured and computed COD's along the stable crack surface was good.

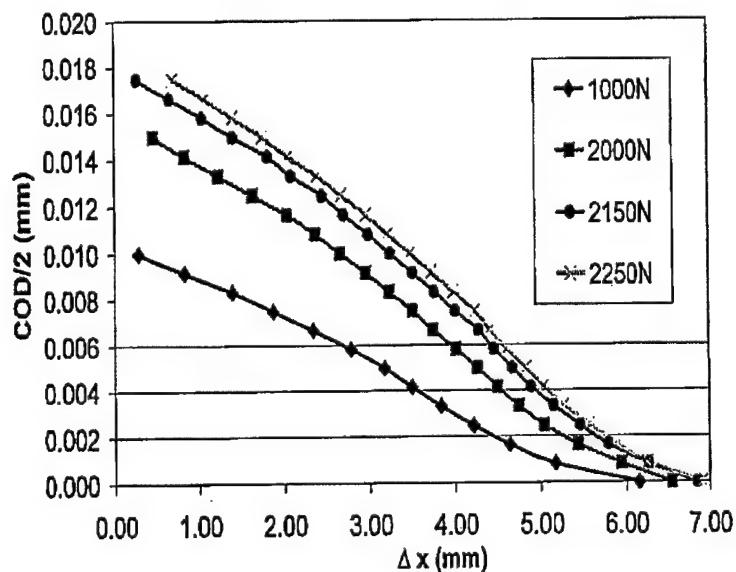


Fig. 3.18. Crack opening profile with crack extension of a monotonic loaded CFCC-B SEN specimen.

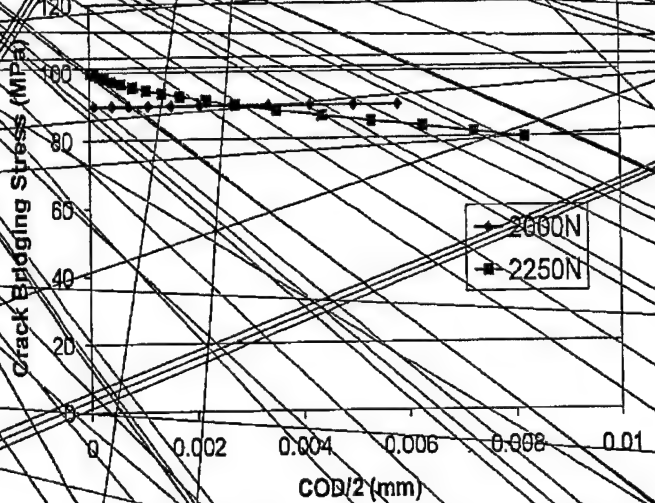


Fig. 3.19. Crack bridging stress versus COD relations of a monotonic loaded CFCC-B SEN specimen.

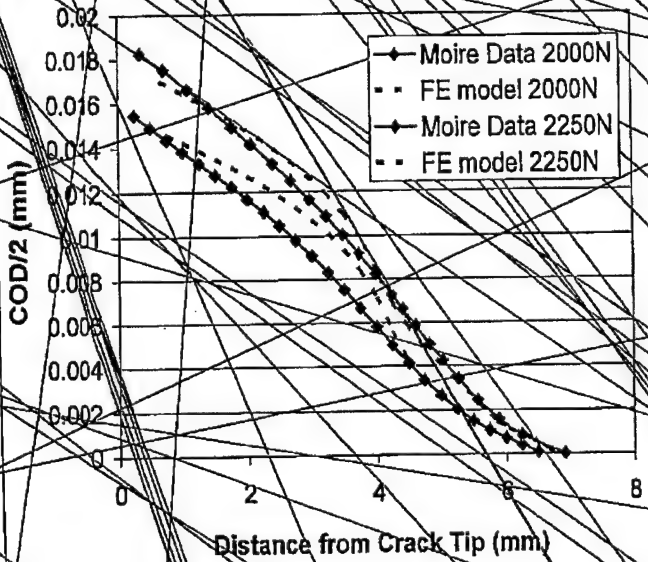


Fig. 3.20. Measured and computed COD in a monotonic loaded CFCC-B SEN specimen.

The CMOD data and the computed displacements of the clamped edge were then used to estimate the load-line displacement which was not measured in this study. The

work of fracture, which is the area underneath the resultant load versus the load line displacement curve was then computed. This work of fracture was 5990 J/m^2 .

Similar analysis of a cyclic loaded CFCC-B SEN were conducted at two load levels with the moiré fringe patterns in Figure 3.12. Figure 3.21 shows the crack opening profile at the two crack extensions. These COD's together with the applied load were used to obtain the crack bridging stress versus COD relation in Figure 3.22 through an inverse FE analysis. The fluctuating crack bridging stresses for the small COD of 0.01 mm is an indication of the sensitivity of moiré interferometry to the discontinuous fracture, which apparently is accentuated under cyclic loading, of the tows. The higher average bridging stress of about 120 MPa in comparison with that of 90 MPa in Figure 3.19 is also reflected in the higher loads in Figure 3.12.

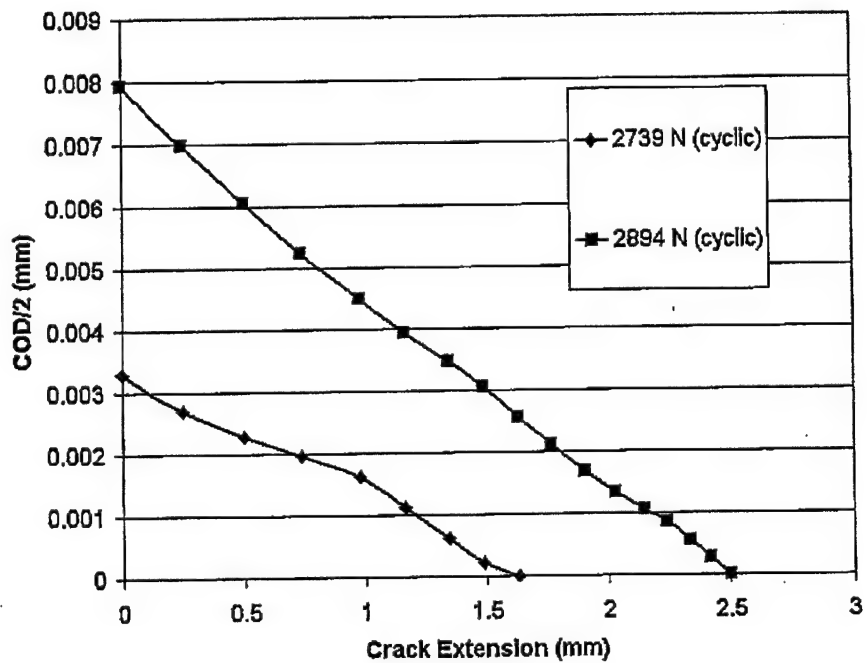


Fig. 3.21. Crack opening profile at a crack extension of $\Delta a = \text{xxx mm}$ in a cyclic loaded CFCC-B SEN specimen.

The work of fracture for the cyclic loaded CFCC-B SEN specimens was 9541 J/m^2 , respectively. This 59% increase in work of fracture of the cyclic loaded CFCC-B SEN specimen could be due to the pseudo work hardening effect of the CFCC-B material under cyclic loading.

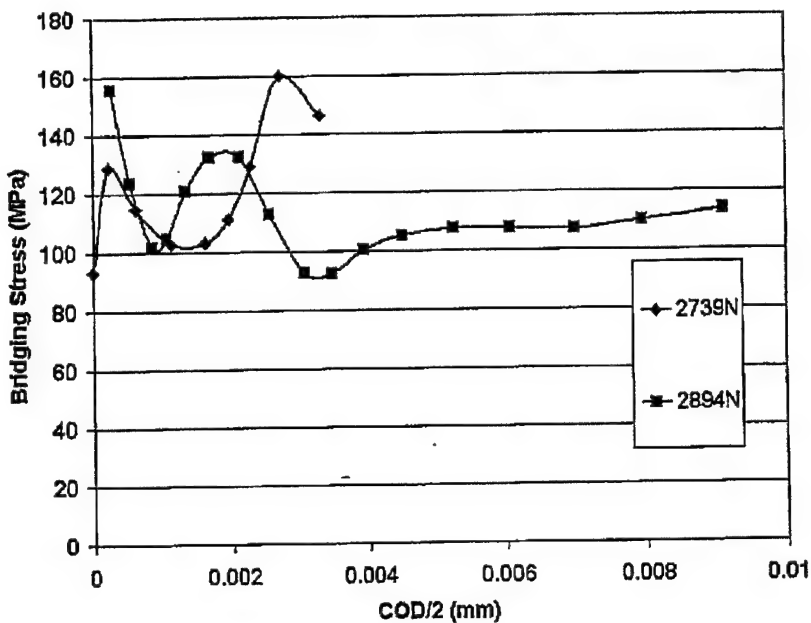


Fig. 3.22. Crack bridging stress versus COD in a cyclic loaded CFCC-B SEN specimen.

3.4. Discussion

The modulus of elasticity, $E_{xy} = 57.6$ GPa used in this study is very closed to that quoted in Reference [19] for the same mullite/alumina composite of CFCC-A. It reports a maximum bridging stress of 11 MPa for a starting COD of about 0.02 mm obtained by post fracture tension (PFT) testing. This corresponds to our bridging stress of 16 MPa in Figure 3.9. This 40 percent difference in the maximum bridging stresses could be due to the fact that the PFT test records predominantly the load carrying capacity of the 0° laminates since the 90° laminates are sheared off at the two PFT specimen surfaces.

3.5. Conclusion

A hybrid experimental/numerical procedure was used to determine the crack bridging forces in a mullite/alumina composite SEN specimen. Cyclic loading resulted in higher load carrying capacity in the CFCC SEN specimens. The work of fracture under monotonic loading of the CFCC SEN specimens with two and four cycles of precursor impregnation and pyrolysis were 6820 and 5990 J/m², respectively. The work of fracture of cyclic loaded CFCC SEN specimen with four cycles of precursor impregnation and pyrolysis was 9541 J/m².

CHAPTER 4: CONCLUSIONS AND RECOMMENDATIONS

4.1. Conclusions

A micro-mechanical FE model, which is based on grain pullout and push-in is presented. The FE model, which was developed through a hybrid experimental-numerical, inverse process, successfully replicated the measured cyclic load and unload relations of an alumina WL-DCB specimen.

Optimization study based on the crack bridging forces showed that Al_2O_3 with all 5 μm grain provided the largest K_{IC} of 3.4 MPa $\sqrt{\text{m}}$ and 2.81 MPa $\sqrt{\text{m}}$ at room temperature and 800°C, respectively.

A hybrid experimental-numerical, inverse procedure was used to model the crack bridging stress of the tortuous crack in a C/C composite SENB specimen.

The measured work rate of fracture was found to be nearly equal to the strain energy release rate obtained from the stress intensity factor of a carbon/carbon composite SENB specimen.

A hybrid experimental/numerical procedure was used to determine the crack bridging forces in a mullite/alumina composite SEN specimen. The work of fracture under monotonic loading of the CFCC SEN specimens with two and four cycles of precursor impregnation and pyrolysis were 6820 and 5990 J/m², respectively. The work of fracture of cyclic loaded CFCC SEN specimen with four cycles of precursor impregnation and pyrolysis was 9541 J/m².

4.2. Recommendation

The hybrid moiré-FE analysis can be used effectively to establish a phenomenological fracture model of the complex failure of ceramic composites. This model should be used to develop an optimization methodology for the design of ceramic composite, similar to the procedure developed for monolithic ceramics as described in Chapter 2 of this report.

REFERENCES

1. Knehans, K. and Steinbrech, R.W. *Memory effect of crack resistance during slow crack growth in notched Al₂O₃ bend specimens*, Journal of Material Science Letters, 1 (8), pp. 327-329, 1982.
2. Hay, J.C. and White, K.W. *Grain Boundary Phases and Wake Zone Characterization in Monolithic Alumina*, Journal of American Ceramic Society, 78 pp. 1025-1032, 1995.
3. Tran, D.T., Yu, C.T., Hay, J.C., White, K.W. and Kobayashi, A.S. "Process Zone Modeling of Polycrystalline Alumina." In: Fracture Mechanics of Ceramics 11, R.C. Bradt, D.P.H. Hasselman, D. Munz, M. Sakai and V. Ya Shevchenko (Eds.), Plenum Publishing Corp, New York, pp. 29-38, 1996.
4. Kokaly, M.T., Tran, D.K., Kobayashi, A.S., Dai, X., Patel, K. and White, K.W. "Modeling of Grain Pullout Forces in Polycrystalline Alumina," Material Science and Engineering. A285, pp.151-157, 2000.
5. Kokaly, M.T., Kobayashi, A.S. and White, K.W. "Modeling of Grain Pullout in Fatigued Polycrystalline Alumina." In: Inverse Problems in Engineering Mechanics III, M. Tanaka and G.S. Dulikravich (Eds). Elsevier Science Ltd, Oxford, pp. 145-152, 2002.
6. Kokaly, M.T., Kobayashi, A.S. and White, K.W. "Fatigue Crack Growth Mechanism in Alumina at High Temperature." In: Fatigue and Fracture Mechanics: 33rd Volume, ASTM STP 1417, pp. 510-523; R.S. Piascik and W.G. Walter (Eds), ASTM International, West Conshohocken, PA, pp. 145-152, 2002.
7. Wang, Y.-L. and Nair, S. "Toughening Behavior of a Two-Dimensional SiC/SiC Woven Composite at Ambient Temperature: II, Stress-Displacement relationship in the Crack Process Zone," Journal of American Ceramic Society, 81 (5), pp. 1157-1162, 1998.
8. Lucchesi, A.J., Hay, J.C. and White, K.W. "Characterization of Wake-Zone Tractions in an Oxidation-Inhibited Carbon/Carbon Composite," Composite Science and Technology, 49, pp. 315-325, 1993.
9. Grimes, R.E. and White, K.W. "Effect of Fiber Architecture on High Temperature Fracture Behavior of 2-D Carbon/Carbon Composites," Mechanics and Mechanism of Damage in Composites and Multi-Materials, ESIS, D. Baptise, (Ed.), pp. 33-44, 1999.
10. Jahanmir, S. and Dong, X. "Mechanism of Mild to Severe Wear Transition in Alpha-Alumina," Journal of Tribology, 114, pp. 403-411, 1992.
11. Ohtake, Y., Sato, S., Hatanaka, K., Masumoto, H., Matsumura, Y. "Biaxial deformation behaviors of C/C composite at high temperatures," Proceedings of International Conference on Advanced Technology in Experimental Mechanics '99 (ATEM '99), 2, pp. 490-495, 1999.
12. Srawley, J.E. "Wide Range Stress Intensity Factor Expressions for ASTM E399 Standard Fracture Toughness Specimens," International Journal of Fracture, 12, pp. 475-476, 1976.

13. Mattoni, M., Yang, J-Y., Levi, C.G. and Zok, F.W. "Effects of matrix porosity on the mechanical properties of a porous-matrix, all-oxide ceramic composite," Journal of American Ceramic Society, v 84, n 11, pp. 2594-2602 , November, 2001.
14. Haslam, J.J., Berroth, K.E. and Lange, F.F. "Processing and properties of an all-oxide composite with a porous matrix," Journal of European Ceramic Society, Vol. 20, pp. 607-618, 2000.
15. Heathcote, J.A., Gong, X.-Y., Yang, J.Y., Ramamurty, U. and Zok, F.W. "In-plane mechanical properties of an all-oxide ceramic composite," Journal of American Ceramic Society, Vol. 82, pp. 2721-2730, 1999.
16. Levi, C.G., Yang, J.Y., Dalgleish, B.J., Zok, F.W. and Evans, A.G. "The Processing and performance of an All-Oxide Ceramic Composite," Journal of American Ceramic Society, v 81, pp. 2077-2086 , 1998.
17. Zok, F. W. and Levi, C.G. "Mechanical properties of porous-matrix ceramic composites," Advanced Engineering Materials, Vol. 3, No. 1-2, pp. 15-22, 2001
18. Tran, D.K., Kobayashi, A.S. and White, K.W., "Crack growth in alumina at high temperature," Engineering Fracture Mechanics, Vol. 68 (2), pp. 149-161, 2001.
19. Souich, Nicholas du. "Wake Zone and Interfacial behavior of two porous Oxide/Oxide Ceramic Matrix Composite," MS thesis submitted to University of Houston, March 2003.

**Crack Bridging and Fracture Zone Characterization of
Oxide/Oxide Ceramic Matrix Composites at Room and
Elevated Temperature**

**Principal Investigator: Dr. Ken W. White, U of H
Co PI: Dr. Albert S. Kobayashi, Univ. of Washington**

**University of Houston
4800 Calhoun Rd.
Houston, TX 77204**

Agreement Number: F49620-01-1-0143

**Crack Bridging and Fracture Zone Characterization of
Oxide/Oxide Ceramic Matrix Composites at Room and
Elevated Temperature**

Ken White

**University of Houston Department of Mechanical Engineering
December 20, 2004**

1.0 Crack Bridging and Fracture Zone Characterization of Oxide/Oxide Ceramic Matrix Composites at Room and Elevated Temperature

1.1 All-Oxide Ceramic Matrix Composites.

Elevated temperature applications require materials that can maintain good mechanical properties such as strength and hardness. Ceramics have good mechanical properties at high temperature, and thus, appear to be good candidates for elevated temperature applications. However, due to their brittle nature, monolithic ceramics are unsuitable for many applications where reliability is very important. Fiber-reinforced ceramic matrix composites (CMCs) exhibit pseudo-plastic behavior at room temperature as well as in elevated temperature environments. In addition, All-Oxide CMCs show an intrinsic creep and oxidation resistance. Energy dissipation mechanisms have been the focus of research in ceramic matrix composites for several years. In non-oxide fiber-reinforced ceramic matrix composites, improvement in fracture toughness is achieved by deflecting matrix cracks along the fiber/matrix interface. Energy dissipation mechanisms involve fiber debonding and fiber sliding. These composites are known to have a “weak” fiber/matrix interface. On the contrary, all-oxide ceramic matrix composites contain a “strong” interface and a porous matrix. Although overall mechanisms and behavior of these new composites are somewhat understood, further studies must be performed in order to understand all the microstructural features and their role on the energy dissipation and fracture behavior during service in harsh environments.

1.2 Materials

Three different materials were considered for this study: an alumina matrix composite [1], and two mullite-alumina matrix composites with the same composition but different level of porosity (CFCC-A 35.5%, CFCC-B 31%) [2]. All composites were reinforced by Nextel 720 oxide fiber cloth (8 harness satin weave). Matrix composition

and the porosity level are important factors responsible for different fracture behavior both at room and elevated temperature.

1.3 Experimental Procedure

In order to analyze the crack bridging mechanisms and the mechanical fatigue response of these composites, full isolation of the wake zone without damaging the wake elements is required. Double Cantilever Beam (DCB) geometry provided the ideal conditions to introduce a controlled matrix crack into the composite. A Post-Fracture Tensile (PFT) experiment was then performed in order to study the bridging phenomenon and the mechanical fatigue behavior. Load vs. displacement curves obtained from the PFT test show the wake-zone toughening contribution and it is related to microstructural features. PFT experiments have shown the role of the microstructural wake-zone toughening features as a function of crack opening displacement (COD). Double cantilever beam geometry provides a large range of COD values for PFT specimens, therefore imposing different stress states on each PFT [3]. It has been shown that the maximum bridging stress is reduced monotonically with increasing initial COD, and the behavior is attributed to an increased damage zone size [3,4,5]. Since interfacial bonding strength and debonded and sliding fiber zones are the controlling mechanisms that provide toughening and lead to a pseudo-plastic behavior in fiber-reinforced ceramic matrix composites, a relationship between maximum bridging stress and COD is of great importance for design [3].

Crack opening displacements during the PFT tests were measured by a video extensometer due to the large displacements of these composites under tensile loading compared to monolithic ceramics.

1.3.1 DCB Specimen

DCB specimens are cut from bulk plates of the ceramic matrix composites. The dimensions of the DCB are 25.4 mm * 50 mm * 3.2 mm. A chevron notch of 13 mm length was made to promote crack initiation. A double side groove was also cut along the crack plane to assure symmetric and stable crack growth. Each side groove has a depth of

one third of the total thickness. A schematic figure of the DCB specimen is shown in Figure 1.

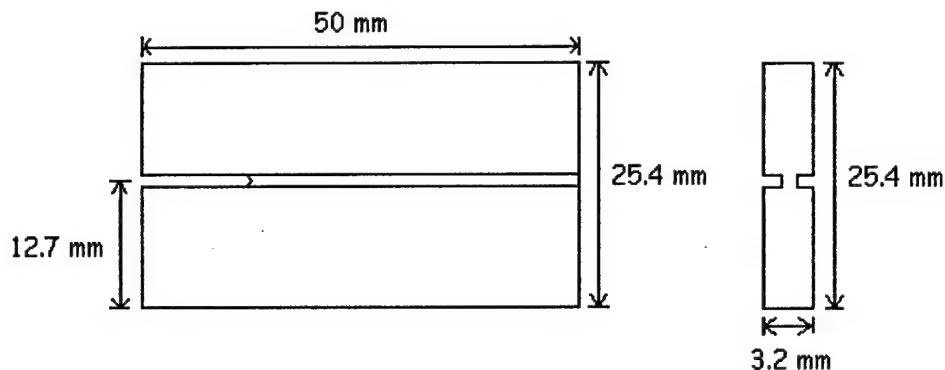


Figure 1 Schematic representation of Double Cantilever Beam specimen

DCB specimens were tested under a tensile loading test. Direct loading on the DCB specimen was first tried without success due to the fracture of loading points. Since these ceramic matrix composites delaminate relatively easily, adhering alumina bars onto the DCB sides also failed. The use of aluminum fixtures to support the DCB and to provide loading points for the DCB specimens gave good results. A diagram of the aluminum fixtures is shown in Figure 2.

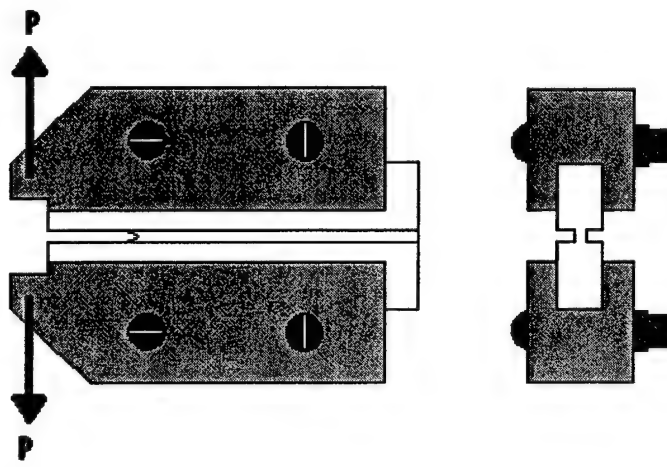


Figure 2 DCB testing fixtures

DCB tension test was carried out in an Instron 4505 twin-screw machine. Two knife-edged fixtures were attached to the Instron in order to pull the DCB specimen apart as shown in Figure 3. The crosshead speed was set to 200×10^{-6} inch/min. Crack propagation along the centered groove was tracked optically. Further crack growth was prevented by load removal after crack length was about 12 to 14 mm. Load and displacement data was collected in real-time through a LabView 5.1 virtual instrument program.

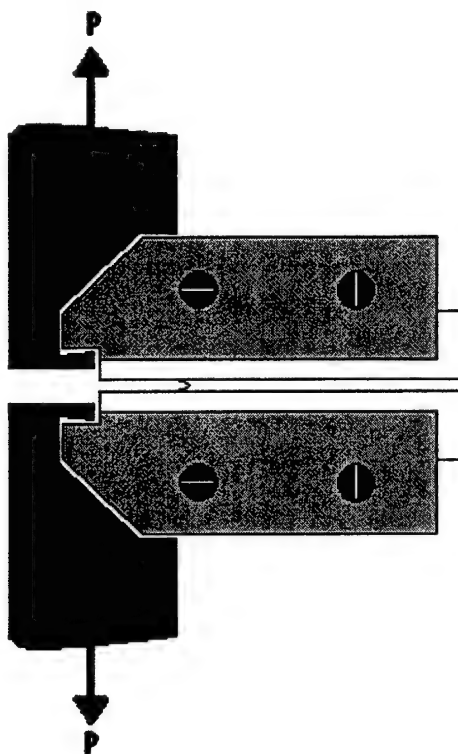


Figure 3 DCB Loading Fixtures

After the DCB test, crack path observations were done using an optical microscope. Since the DCB test was only used to create an initial crack in order to study the wake zone behavior, this test was only performed at room temperature.

1.3.2 PFT Specimen

PFT specimens were obtained from tested DCB specimens. The DCB crack length was tracked using optical microscopy to locate the end of wake zone. Isolated

wake zone elements are obtained by cutting the DCB specimen into several PFT specimens as shown in Figure 4.

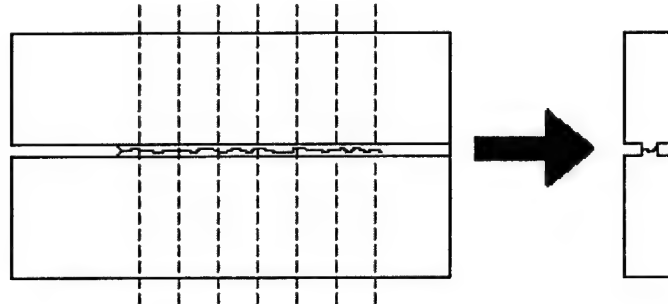


Figure 4 PFT specimens obtained from DCB sample

Since PFT specimens are obtained from a cracked DCB along the groove, PFT specimens are only held together by bridging elements. In addition, each PFT specimen contains a unique section of the wake zone, i.e. different crack opening displacement for each specimen. PFT specimens are numbered according to their position with respect to the opposite end from the chevron notch.

The PFT specimen is glued to alumina bars in a double-T fashion to facilitate a tensile test. Due to its property retention up to 1650 °C, Resbond 989, an alumina-based high temperature adhesive produced by Cotronics, Inc., was used to glue the PFT specimens to the alumina bars. Two short and thin silicon carbide bars acted as the video extensometer targets. Figure 5 shows the PFT specimen ready to be tested.



Figure 5 Post-Fracture Tensile Test Specimen with video extensometer targets

Monotonic loading of the PFT specimens was carried out by motion of the Instron crosshead. However, for cyclic loading, a piezo actuator was fixed to the Instron machine

and used as the cyclic mechanism. The piezo actuator required a high voltage power supply (0 – 800 V) to give a cyclic amplitude of 0 to 55 μm .

1.4 DCB Test

As expected from the factor of difference between the elastic moduli of the two compounds, the alumina matrix composite exhibits a higher stiffness as well as a higher load capacity than the CFCC-B mullite-alumina matrix composite. Alumina has an elastic modulus of 370 GPa while for mullite, this value is 150 GPa. By using the rule of mixtures, the elastic modulus for the alumina matrix composite gave a value of 317 GPa, while for the mullite-alumina composite (CFCC-A) the value was 218 GPa. Furthermore, the alumina matrix composite shows a higher maximum load for crack initiation. Another important feature of these two composites is the absence of catastrophic failure after the peak stress is reached and a crack starts propagating. Figure 6 shows the DCB response for these composites.

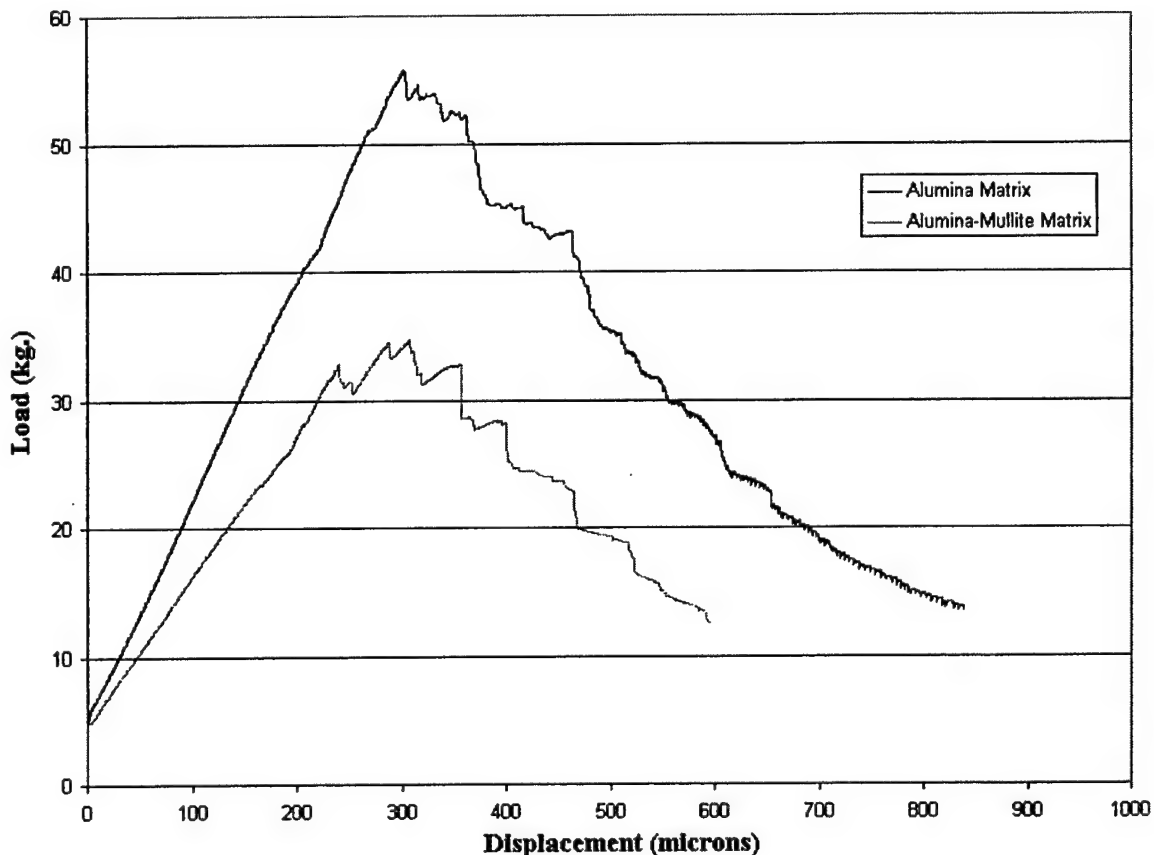


Figure 6 DCB results for the alumina matrix and the mullite-alumina (CFCC-A) matrix composites

A run arrest behavior, previously suggested as a manifestation of bundle fiber pullout in fiber-reinforced composites [6], can be observed in the mullite-alumina composite during crack growth suggesting a more severe damage in this composite. Further analysis under Scanning Electron Microscope (SEM) after PFT tests showed evidence of bundle pullout for both composites with the mullite-alumina matrix, while for the alumina composite single fiber pullout dominated. Figure 7 shows SEM images of the fracture surface of the mullite-alumina composites.

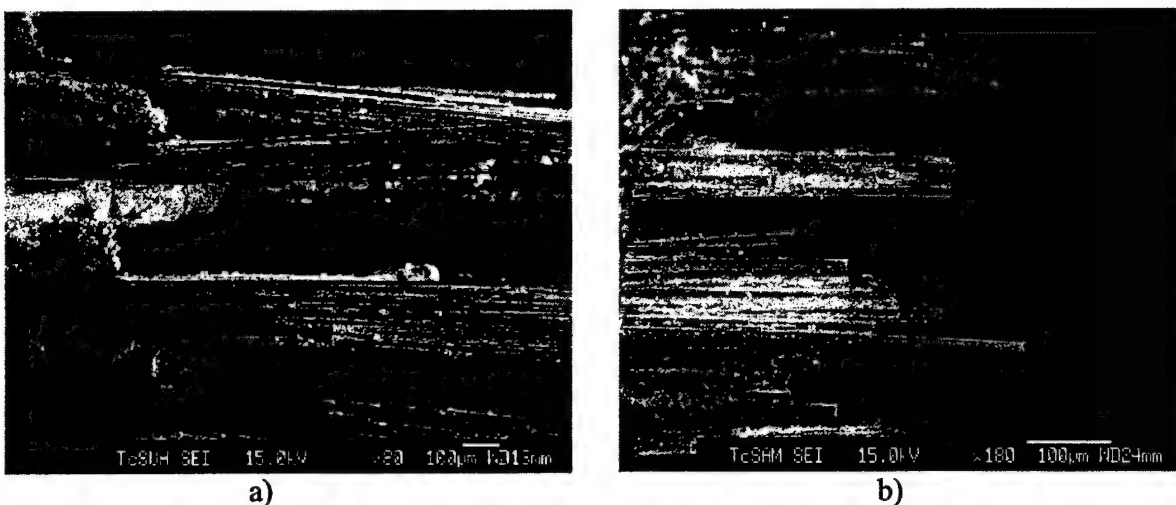


Figure 7 Fracture surfaces of the mullite-alumina composites after monotonic PFT tests:
a) CFCC-B at room temperature. b) CFCC-A at 1000 °C

An initial value, K_0 , and the steady-state fracture toughness, K_s , were obtained for the alumina matrix and for the mullite-alumina (CFCC-A) matrix composite by using the LEFM model. Both materials exhibit fracture toughness values comparable to those of some metals. An increase in fracture toughness from the initial value to the steady-state region suggests a rising R-curve for both composites. The initial fracture toughness for the alumina matrix composite is about $38 \text{ MPa m}^{1/2}$, while for the alumina/mullite composite is about $23 \text{ MPa m}^{1/2}$. The steady-state toughness for both materials was higher than that for initiation suggesting the existence of a rising R-curve. For the

alumina composite, the steady-state toughness increased to $66 \text{ MPa m}^{1/2}$, whereas the alumina/mullite matrix composite reached plateau at about $47 \text{ MPa m}^{1/2}$.

1.5 PFT Tests

The PFT specimens obtained from each DCB specimen were characterized by their initial crack opening displacement (COD) characteristic of the crack opening profile. Table 1 characterizes this COD profile for both composites. These values were used to characterize the initial damage in the PFT specimen.

PFT Specimen Number	1	2	3	4	5	6	7	8
Distance from DCB crack tip (mm)	0	2.54	5.08	7.62	10.16	12.7	15.24	17.18
COD (μm)	45	65	95	120	145	180	215	245

Table 1 Typical COD values for PFT specimens of both composites.

Different PFT specimens taken from the same DCB (family of PFTs), each representing an increasing level of prior damage (initial COD) with distance from the DCB crack tip, showed a decreasing maximum bridging stress. In addition, the PFT specimens of a family exhibit a common strain-softening exponent both at room and elevated temperature. Loading and reloading sequences were carried out and confirmed this behavior. The drop in sustained load (stress) with increasing COD reflects both the number of reduced load-bearing fibers and the reduced fiber matrix interaction. Figures 8, 9, and 10 show families of PFT for different composites and testing temperatures.

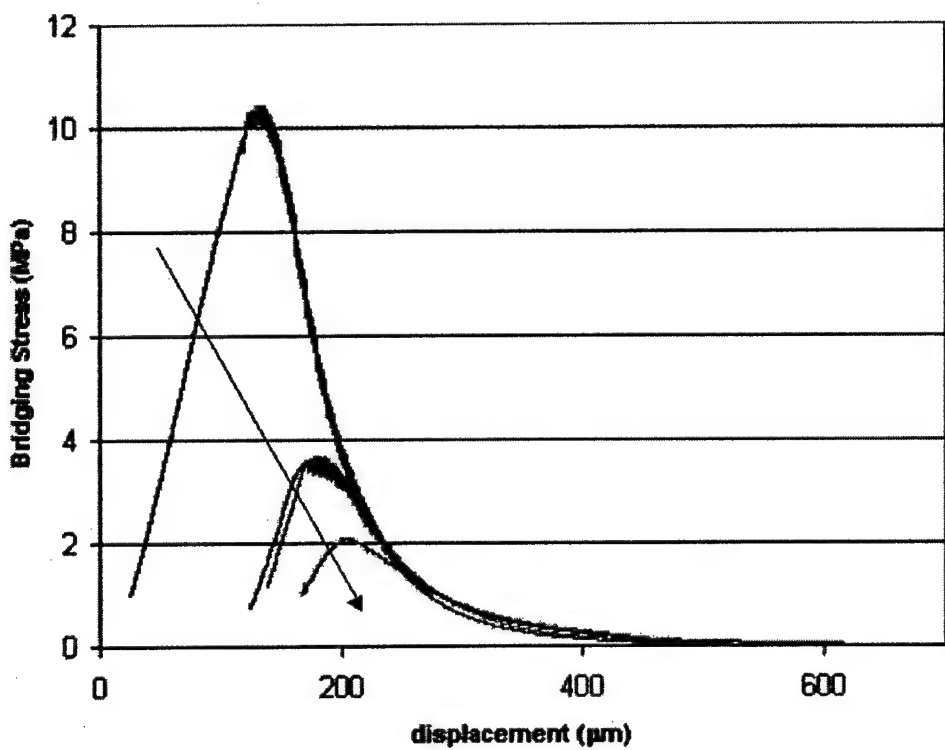


Figure 8 Family of PFT curves of the mullite-alumina (CFCC-B) matrix composite at room temperature.

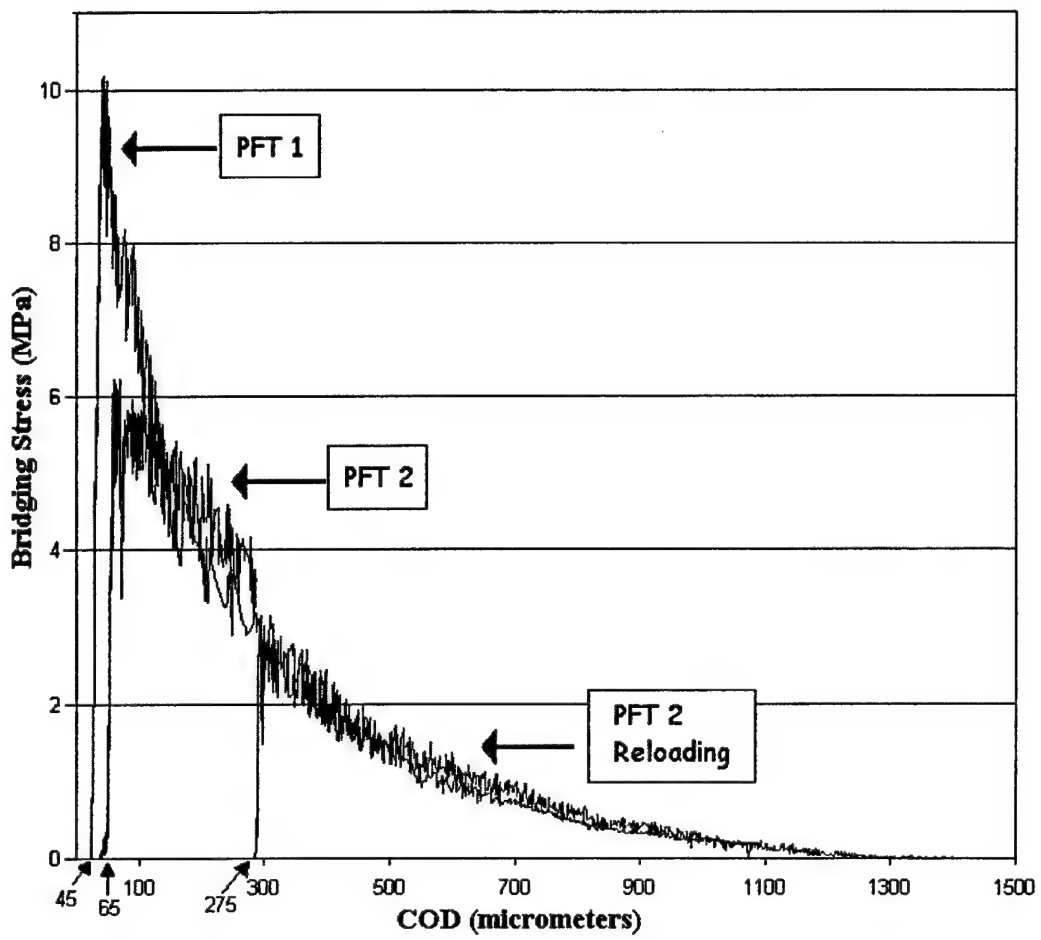


Figure 9 Family of PFT curves for the alumina matrix composite at 1000 °C.

The modest change in elastic stiffness of the loading curves for the alumina matrix composite (Figure 9) suggests a relatively low and individual fiber breakage, but strengthens the argument for load loss due to interfacial or matrix damage. Furthermore, the oscillating behavior of the load throughout the strain-softening region and its reduced amplitude in the final stages of the separation event suggests a high dependence on interfacial properties.

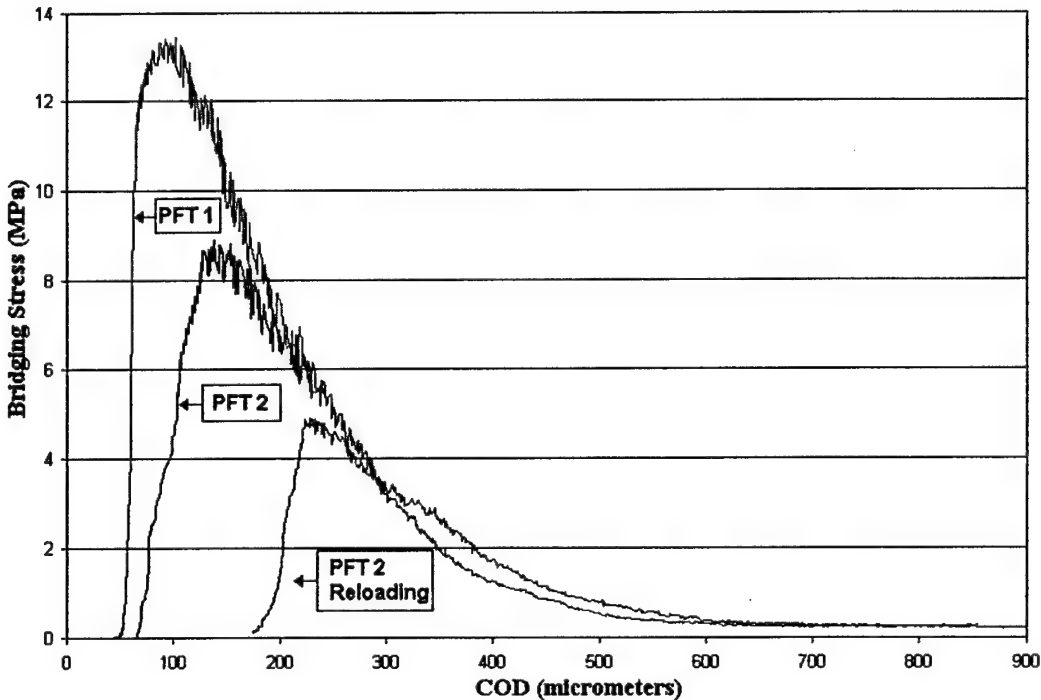


Figure 10 Family of PFT curves for the mullite-alumina (CFCC-A) matrix composite at 1000 °C.

1.5.1 Room vs. Elevated Temperature Testing

The shape of the pseudo-plastic region remained unchanged between room to elevated temperature testing, confirming the strain-softening region. Furthermore, the linear region was also unchanged reflecting the good temperature resistance of the fibers, and the existence of a suitable load-transferring fiber/matrix interface. Figure 11 shows the mechanical response at room and 1000 °C of the alumina matrix composite. However, a noticeable effect of temperature on the stick-slip behavior during fiber pullout was observed. Previous studies suggest a similar behavior caused by interfacial roughness [7-8]. Further SEM analysis showed large amounts of matrix material attached to the pulled out fibers (Figure 12) after temperature exposure, explaining the increased interfacial roughness and suggesting a temperature-driven adhesion (probably through sintering) of matrix material to the fibers.

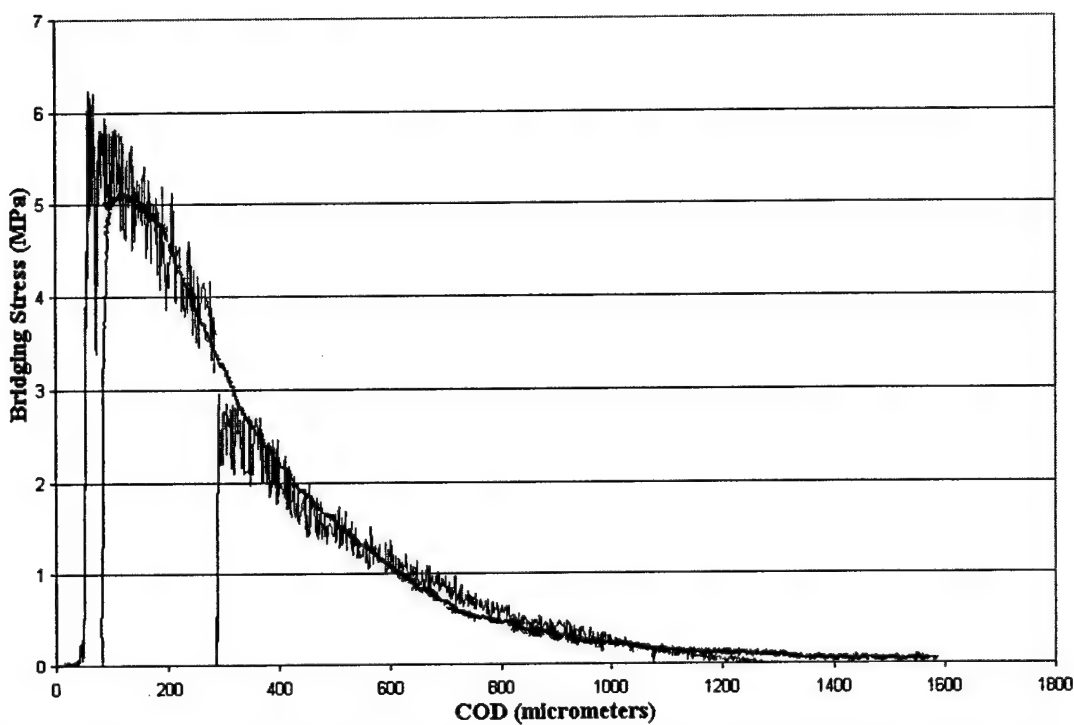


Figure 11 Room (PFT-3) vs. High temperature (PFT-2) behavior of the alumina matrix composite.

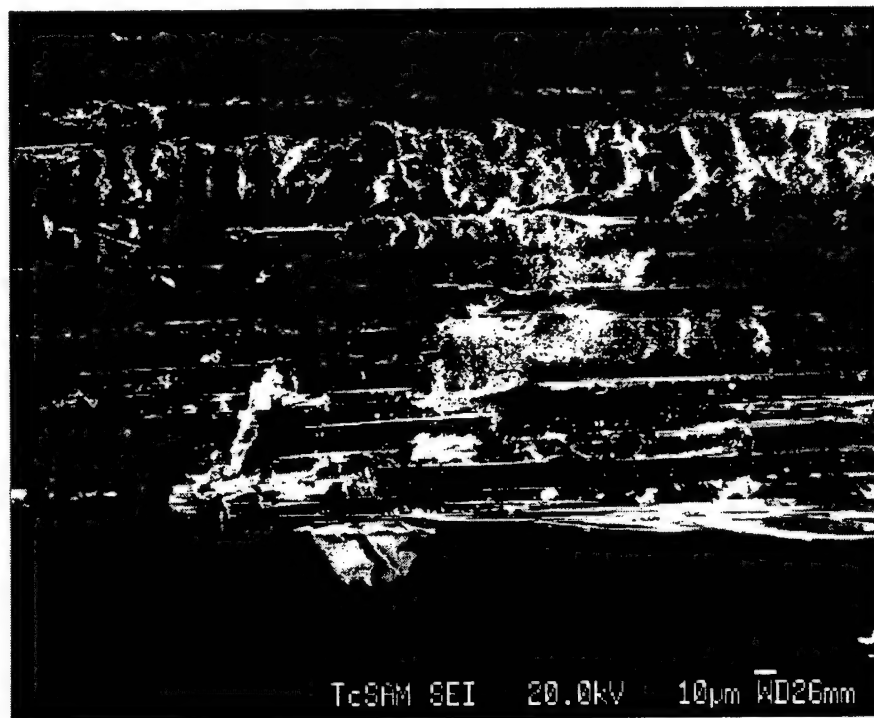


Figure 12 Fiber pullout of the alumina matrix composite under monotonic loading at 1000°.

A similar oscillating load behavior to that of the alumina matrix composite was found for the mullite-alumina (CFCC-A) matrix composite at elevated temperatures. However, the effect was smaller in this composite, suggesting a smoother interface during fiber sliding than that of the alumina matrix composite.

1.5.2 Critical Temperature

A diminished load supporting capacity for the alumina matrix composite began with temperature exposure at about 1000°C, suggesting significant microstructural changes for temperatures above 1000-1100°C. On the other hand, the mullite-alumina (CFCC-A) matrix composite maintained a uniform strength at temperatures below 1200°C, showing the benefits of the mullite content in strength retention. Figures 13 and 14 show the load vs. temperature behavior of the alumina matrix and the mullite-alumina (CFCC-A) matrix composite respectively.

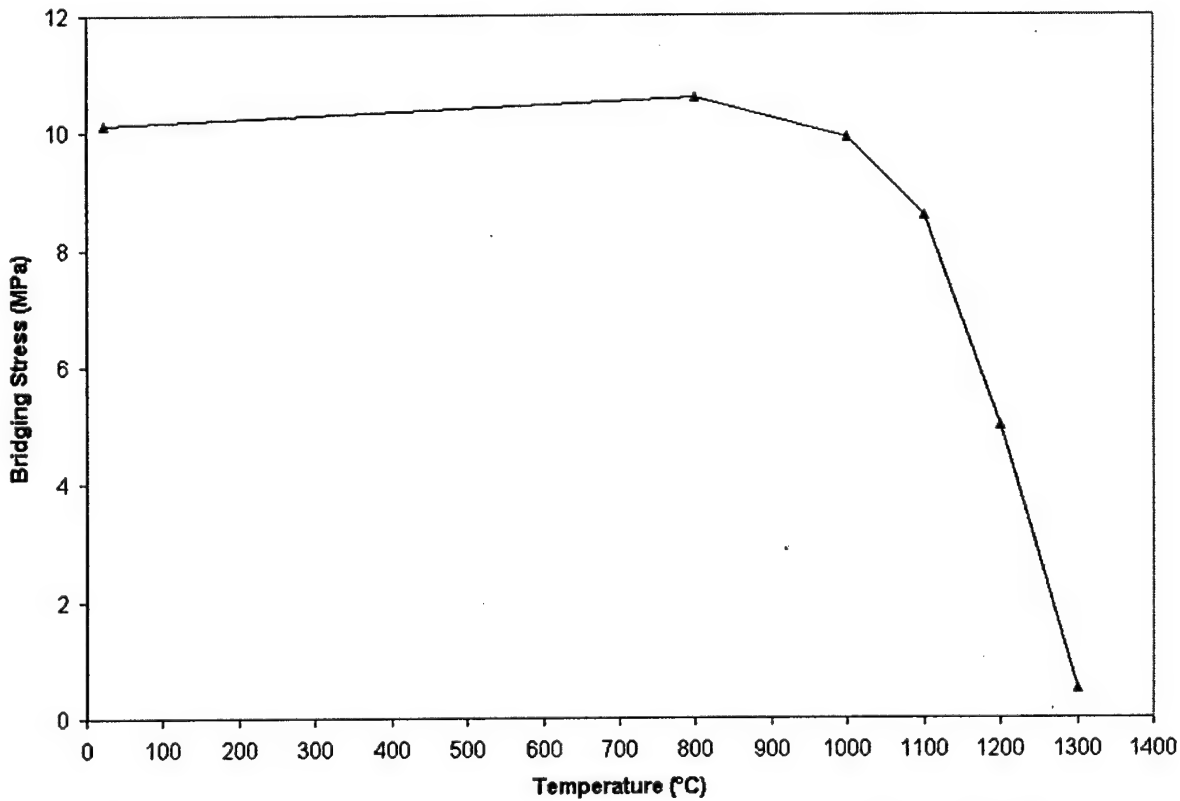


Figure 13 Bridging stress vs. temperature for the alumina matrix composite

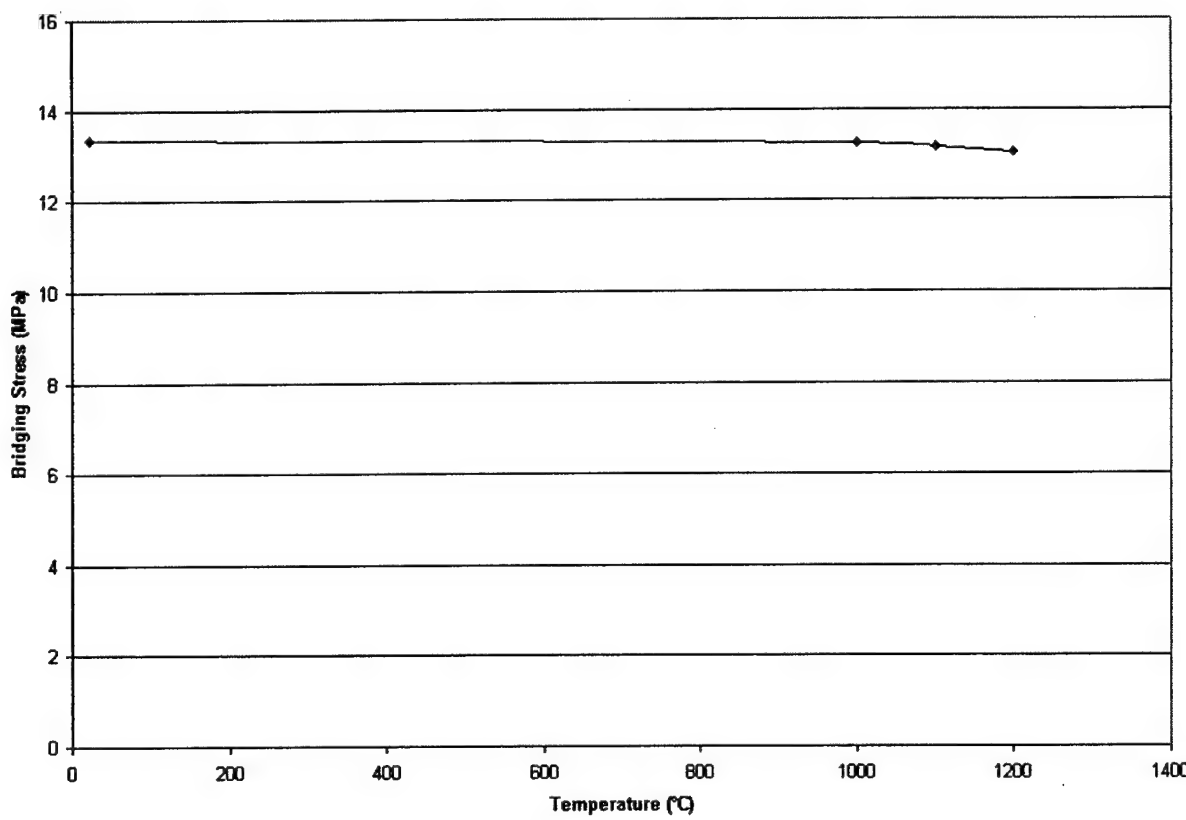


Figure 14 Bridging stress vs. temperature for the mullite-alumina (CFCC-A) matrix composite.

1.5.3 Cyclic Behavior

Cyclic PFT tests were performed on both the alumina matrix and the mullite-alumina (CFCC-B) matrix composites. The appearance of a hysteresis loop (an energy dissipation mechanism) caused by the frictional forces and closely related to the fiber sliding length, as previously suggested before, was characteristic for these composites. Due to the nature of the PFT test, where only tensile loading is possible, the energy required to close the hysteresis loop arises solely from the stored elastic energy, suggesting the existence of enough stick-points acting with sufficient strain energy. Figure 15 shows one an individual loading cycle for the alumina matrix composite.

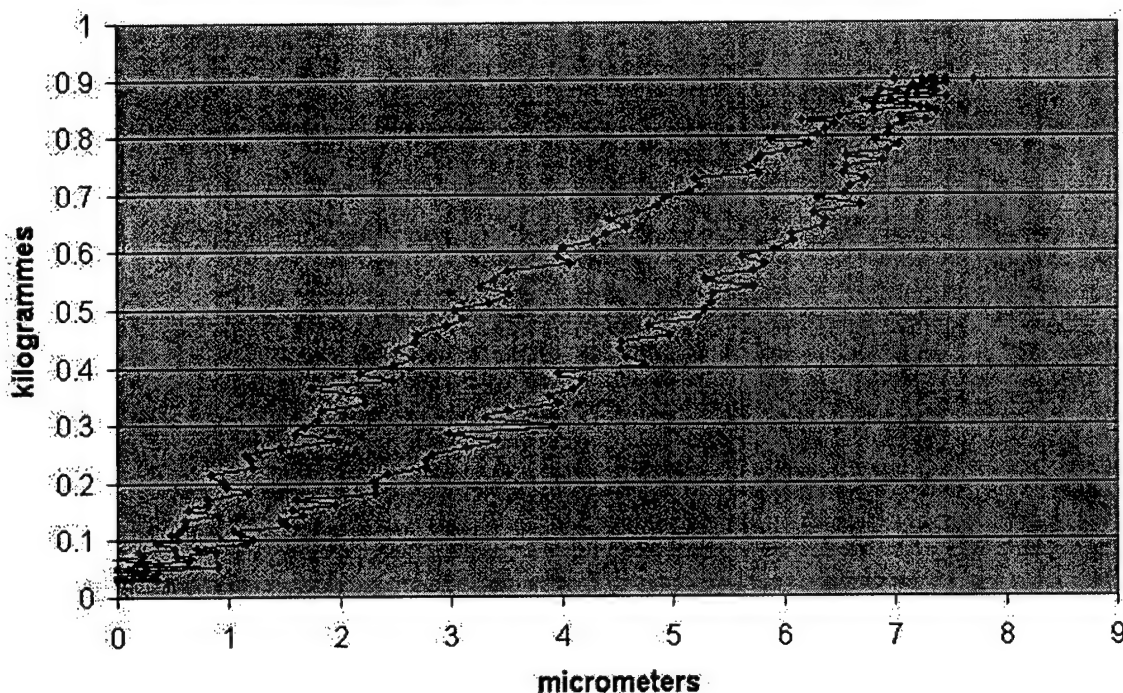


Figure 15 Cyclic PFT of an alumina matrix composite PFT specimen

Although the hysteresis loop fully closes for the configuration shown in Figure 15, Figure 16 shows that further cycling led to non-recoverable displacement at one point. A sharp transition point at the maximum load, suggests a large number of stick points converting to slip contacts therefore inducing gross slip. SEM analysis of cycled samples showed evidence of gross slip (Figure 17). The reduced number of stick points appeared to be caused by interface degradation by frictional forces during cycling, however, once gross slip took place, a new configuration (new portions of fiber sliding) could be reached giving enough stick points to fully close the hysteresis loop again.

On the other hand, consecutive cycles on a PFT specimen showed the need of a higher load to induced gross slip from partial slip. Figure 18 shows this behavior for the mullite-alumina (CFCC-B) matrix composite. This response suggested a great dependence on the fiber/matrix interfacial properties, with the latter providing the frictional forces and contact configurations controlling crack growth during fiber sliding.

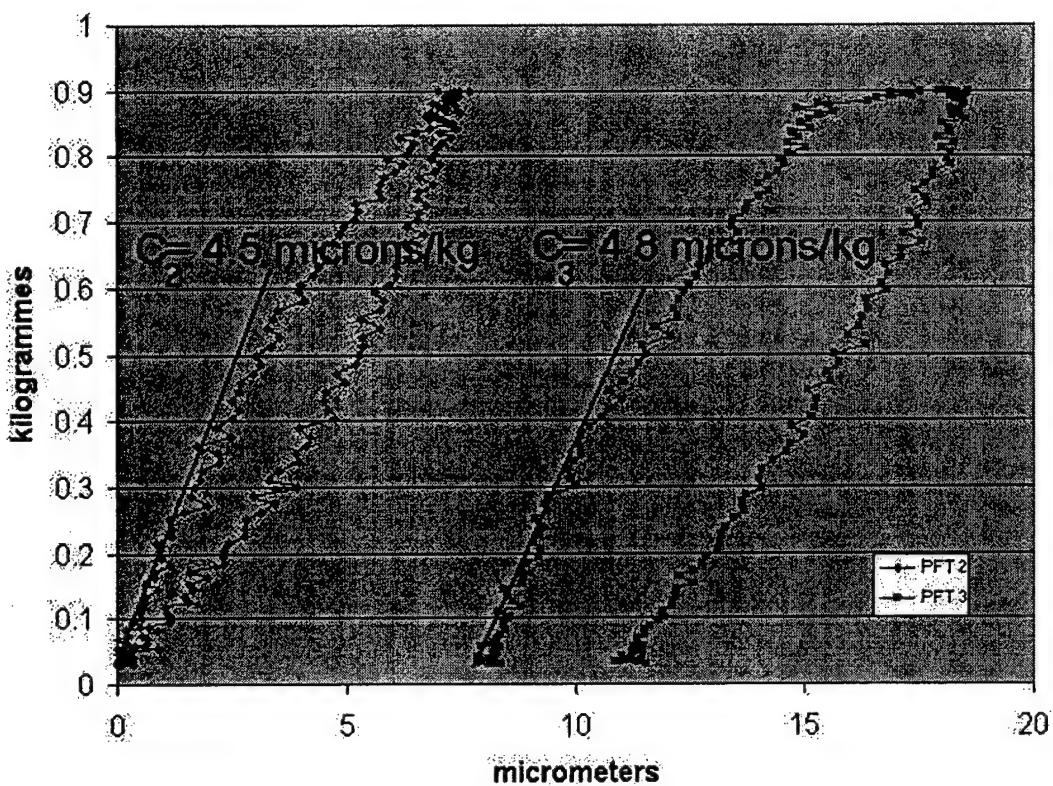


Figure 16 Evidence of gross slip in the alumina matrix composite during cyclic loading.

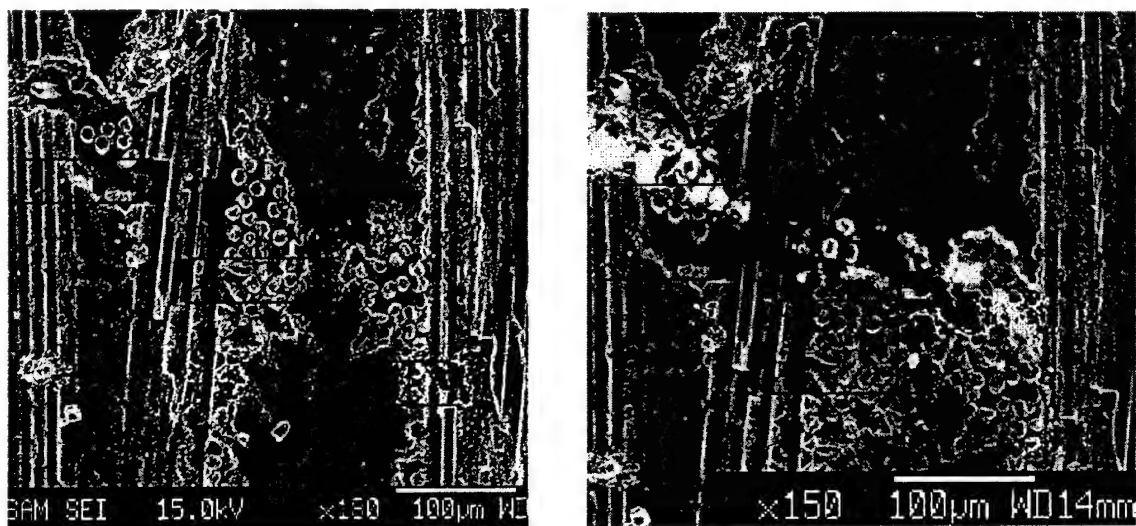


Figure 17 SEM imaging showing gross slip and crack growth

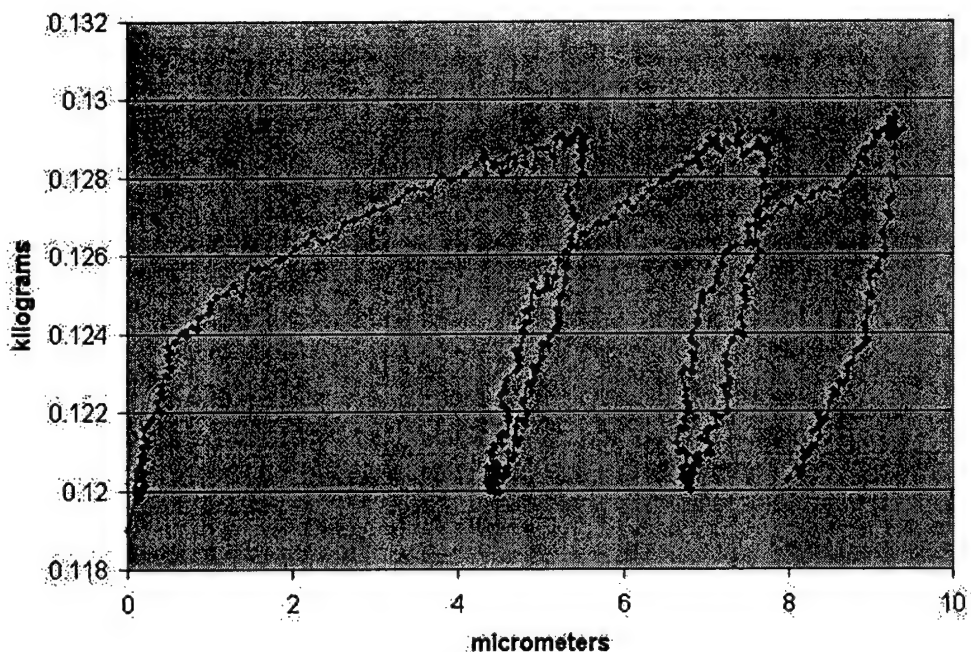


Figure 18 Consecutive cycles for the mullite-alumina (CFCC-B) matrix composite.

The long term fatigue behavior of the composites showed a steadily increasing COD with number of cycles (Figure 19). Wear effects, probably due to friction, on the fiber/matrix interface during cycling caused gross slip and therefore crack growth.

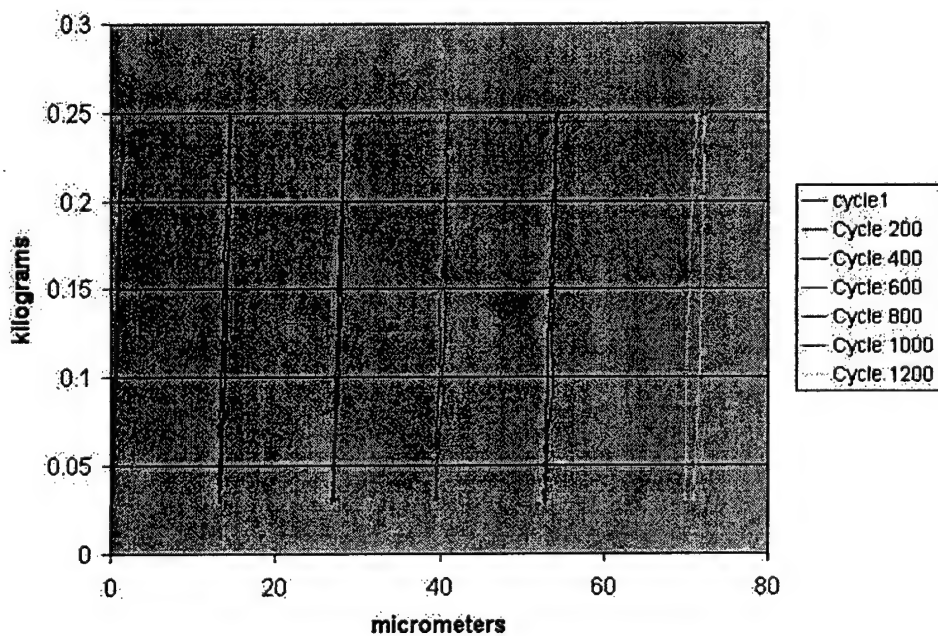


Figure 19 Long term cyclic behavior of the mullite-alumina (CFCC-B) matrix composite.

1.6 Relation between Cyclic and Static (monotonic) PFT tests

A critical relationship between the results obtained under monotonic loading and long-term fatigue behavior was observed for all the composites studied in this investigation. The Static PFT load curve provided a critical failure criterion for fatigue conditions at both room and elevated temperatures. Failure by fatigue was controlled by the critical value of COD given by the Static PFT curve for a given maximum cycling load. Figures 20 and 21 show the failure condition for the alumina matrix and for the matrix composites at room temperature respectively.

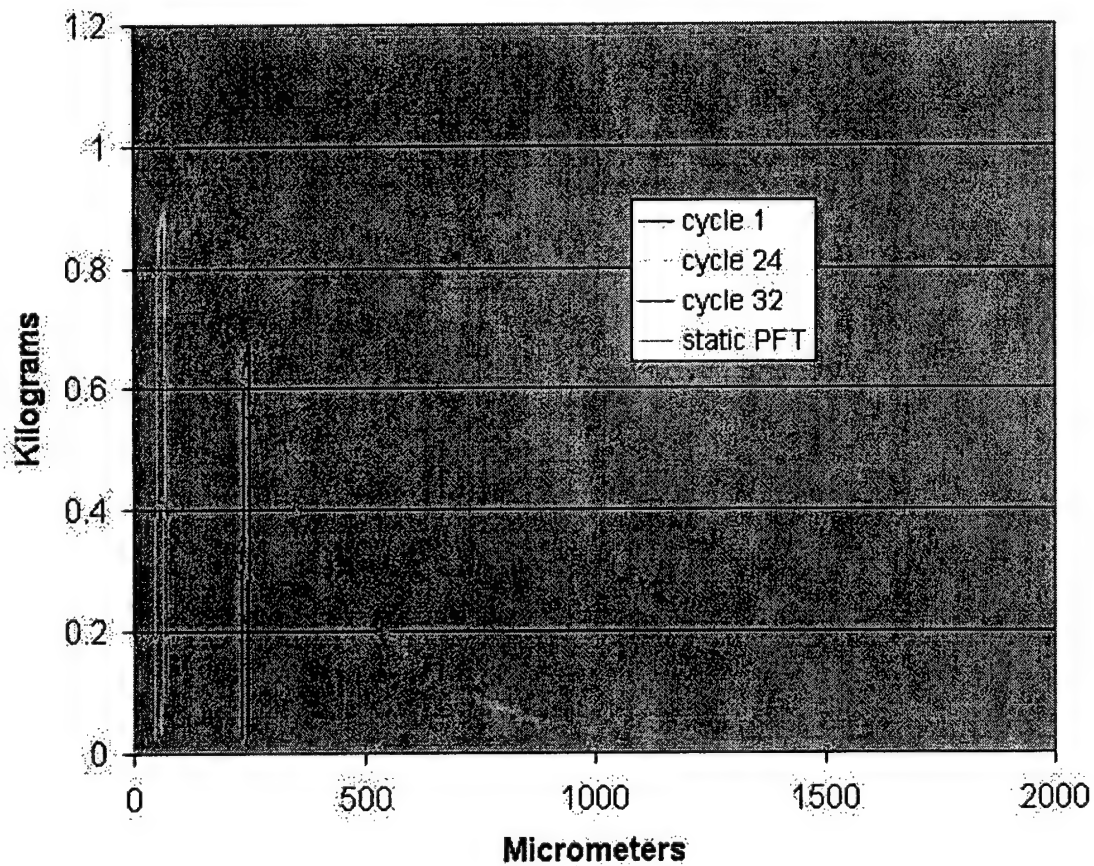


Figure 20 Static PFT curve predicted failure of specimen of the alumina matrix composite under cyclic conditions

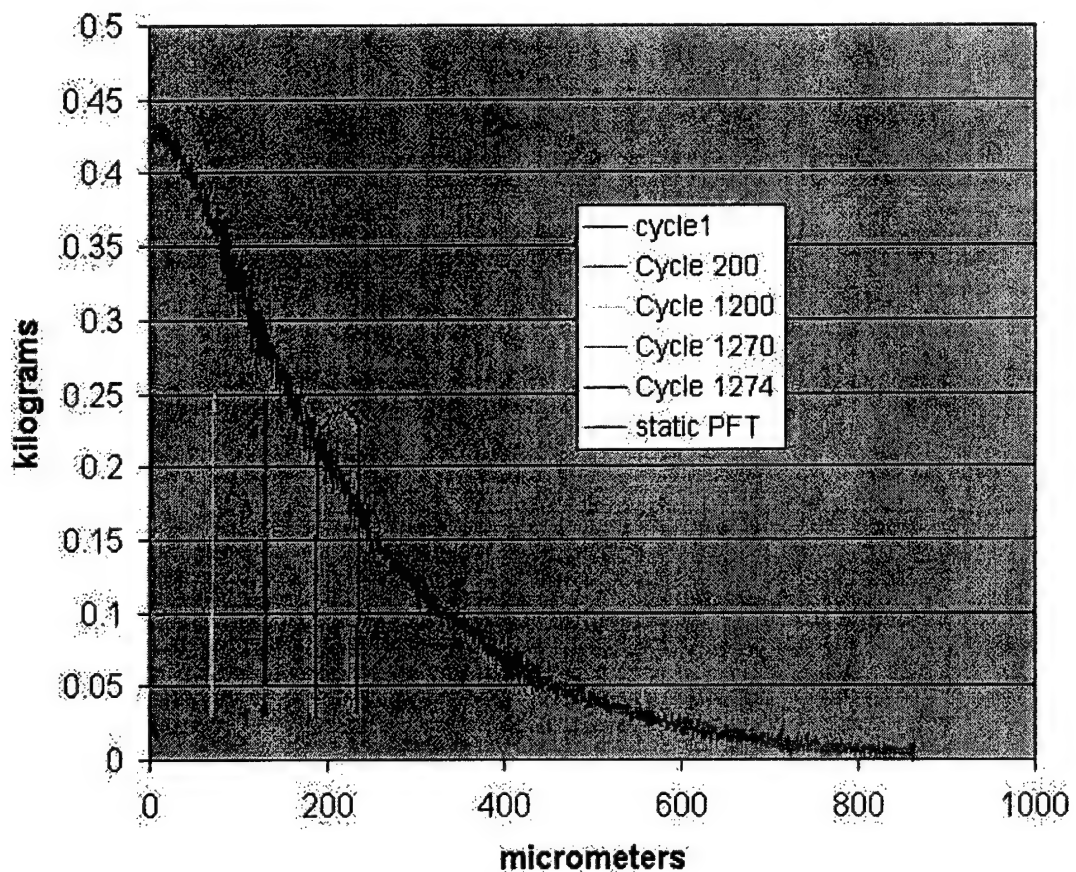


Figure 21 Static PFT curve predicted failure of specimen of the mullite-alumina (CFCC-B) matrix composite under cyclic conditions.

For both materials, failure was observed when the load and COD combination fell outside the monotonic load vs. COD curve. Therefore, fracture of the PFT specimen was controlled by the present crack opening displacement; in other words, damage accumulated on the composite was quantifiable by the resulting increase in COD. This behavior was also observed at elevated temperatures, however, experimental limitations allowed only approximations of COD measurements. Figures 22 and 23 show the cycled region of the alumina matrix and the mullite-alumina (CFCC-A) matrix composites at 1000°C, respectively.

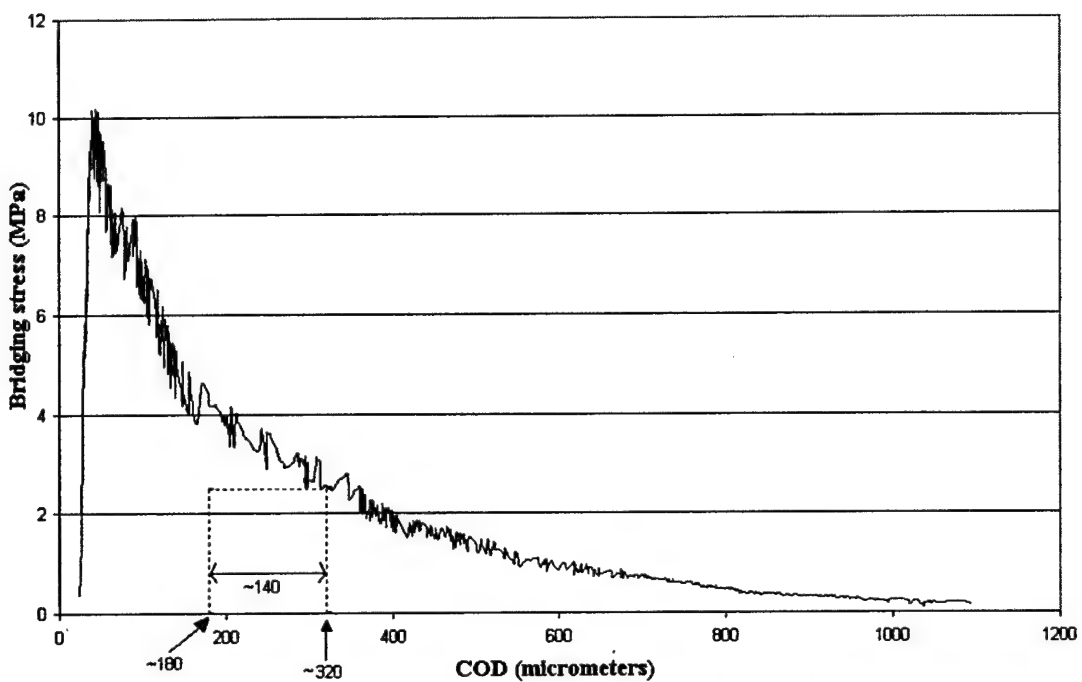


Figure 22 Static vs. Cyclic PFT test for the alumina matrix composite (1000 °C)

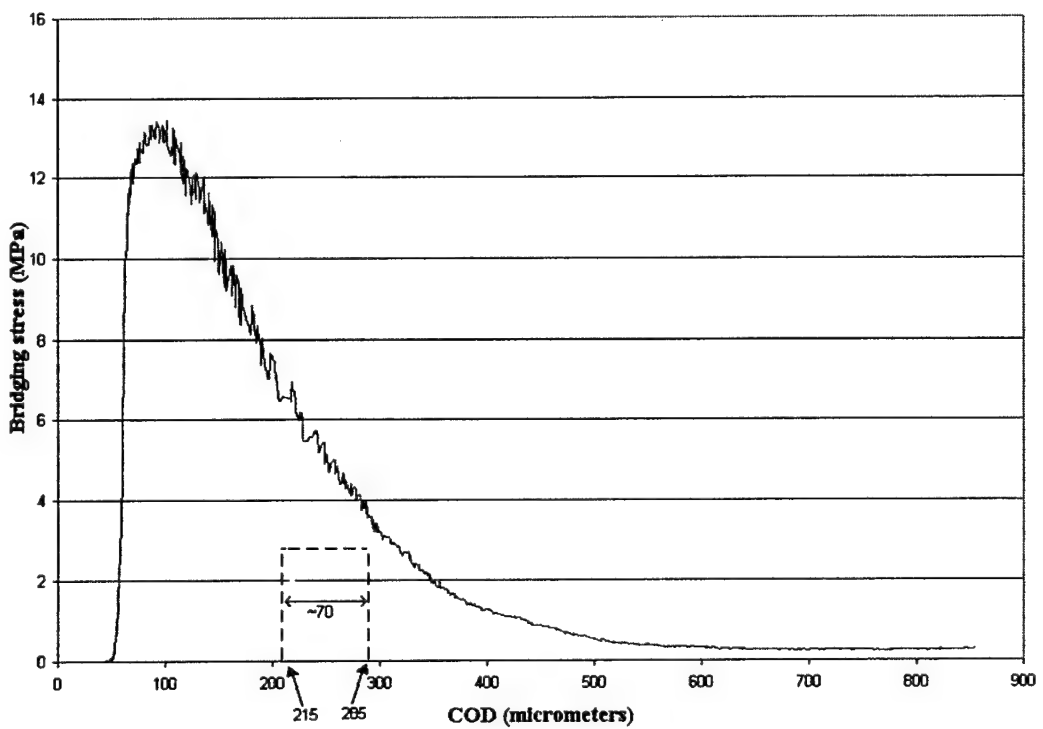


Figure 23 Static vs. Cyclic PFT test for the mullite-alumina (CFCC-A) matrix composite
(1000 °C).

In both cases, failure occurred near the crossing point between the static curve and the cyclic curve, confirming a displacement controlled failure mechanics at elevated temperatures. The Static PFT curve was then proved to predict failure in materials with a displacement controlled failure mechanisms, such as the fiber-reinforced ceramic matrix composites studied in this research.

1.7 Discussion

The results obtained in this study were related to those reported in Reference [9] by an extrapolation of the gathered data. Higher bridging stresses are reported in [9] and compared to the ones obtained in this study. However, the crack opening displacements measured in [9] are considerably smaller than the ones used for the PFT tests, suggesting a required stress of about a 100 MPa for crack initiation (reported in [9]), but lower stresses (~10-15 MPa) for crack propagation obtained by the PFT method.

Temperature exposure up to 1000°C showed no important effect on any of the composites studied, confirming the appealing properties of these composites for high-temperature applications.

The fiber/matrix interfacial properties play a critical role in fracture resistance of these composites, as seen in the mechanical response during fiber sliding and pullout under PFT tests. The fiber/matrix interfacial condition appears to control the number of stick points available for full recovery or partial and/or gross slip during cyclic loading. Frictional interfacial wear was evident in both cyclic and monotonic loading, mainly in the final stages of the separation event, in the form of reduced load-bearing capacity and smoother fiber pullout.

2.0 Conclusions and Recommendations

A unique experimental procedure was used to determine crack bridging stresses, as well as the fiber/matrix interfacial role during fiber sliding and as an active energy dissipation mechanism in fiber-reinforced ceramic matrix composites with all-oxide constituents.

A displacement-controlled failure mechanism dominates in these composites, establishing a useful relationship between accumulated damage and present crack opening displacements for failure prediction under fatigue loading conditions. Microstructural analysis by SEM led to identification of important changes with temperature exposure, allowing the determination of critical service temperatures.

Using the LEFM model, values for fracture toughness comparable to those of some metals were found for these composites.

Experimental data obtained by the PFT method gives a great insight of the mechanical properties of these composites, and can be used to establish a microstructure-processing-properties connection.

REFERENCES

1. <http://www.coiceramics.com/cmcdevelopment.htm> COI Ceramics. San Diego, California, USA.
2. C. G. Levi, J. Y. Yang, B. J. Dalglish, F. W. Zok, and A. G. Evans, "Processing and Performance of an All-Oxide Ceramic Composite," *Journal of the American Ceramic Society* **81**, 2077-2086 (1998).
3. A. J. Lucchesi, J. C. Hay, and K. W. White, "Characterization of Wake-Zone Tractions in an Oxidation-Inhibited Carbon/Carbon Composite," *Composites Science and Technology* **49**, 315-325 (1993).
4. K. W. White and J. C. Hay, "Grain Boundary Phases and Wake Zone Characterization in Monolithic Alumina," *Journal of the American Ceramic Society* **78**, 1025-1032 (1995).
5. J. C. Hay and K. W. White, "Crack Face Bridging Mechanisms in Monolithic MgAl₂O₄ Spinel Microstructures," *Acta Metallurgica and Materialia* **40**, 3017-3025 (1992).
6. J. M. Neumeister, "Bundle Pullout--A Failure Mechanism Limiting the Tensile Strength of Continuous Fiber Reinforced Brittle Matrix Composites--And its Implications for Strength Dependence on Volume and Type of Loading.," *Journal of Mechanics and Physics of Solids* **41**, 1405-1424 (1993).
7. T. J. Mackin, P. D. Warren, and A. G. Evans, "Effects of Fiber Roughness on Interface Sliding in Composites," *Acta Metallurgica and Materialia* **40**, 1251-1257 (1992).
8. J. D. Bright, S. Danchaivijit, and D. K. Shetty, "Interfacial Sliding Friction in Silicon Carbide-Borosilicate Glass Composites: A Comparison of Pullout and Pushout Tests.," *Journal of the American Ceramic Society* **74**, 115-122 (1991).

9. A. S. Kobayashi, "Modeling of Failure in Monolithic and Ceramic Matrix Composite under Static and Cyclic Loading" Final Report submitted to the Air Force Office of Scientific Research. July 15, 2004.